Experimental study of rotating pipe and jet flows

by

Luca Facciolo

November 2003
Technical Reports from
Royal Institute of Technology
Department of Mechanics
S-100 44 Stockholm, Sweden

Akademisk avhandling som med tillstånd av Kungliga Tekniska Högskolan i Stockholm framlägges till offentlig granskning för avläggande av teknologie licentiatsexamen torsdagen den 20:e November 2003 kl 10.00 i Seminarierummet S40, Teknikringen 8, KTH, Stockholm.

Universitetsservice US AB, Stockholm 2003

Alle cose perdute...

Luca Facciolo 2003 Experimental study of rotating pipe and jet flows
KTH Mechanics
S-100 44 Stockholm, Sweden

Abstract

The present study is an experimental investigation on rotating flows. A special facility has been built in order to produce a turbulent swirling jet generated by a fully developed rotating pipe flow. The work is so naturally divided into two main parts: the turbulent rotating pipe flow and the swirling jet.

The turbulent pipe flow has been investigated at the outlet of the pipe both by hot-wire anemometry and LDV. The LDV has been also used to measure the axial velocity component inside the pipe. The research presents the effects of the rotation and Reynolds number ($12000 \leqslant Re \leqslant 33500$) on a turbulent flow providing a theoretical curve for the azimuthal-radial Reynolds stress and comparing the experimental results with theory and simulations. Especially a comparison with the recent theorteical by Oberlack (1999) is made.

The rotating pipe flow also represents the initial condition of the jet. The rotation applied to the jet drastically changes the characteristics of the flow field. The present experiment has been performed mainly for weak swirl numbers ($0 \leqslant S \leqslant 0.5$). All the velocity components and their moments are presented together with spectra along the centerline and entrainment data.

The data from the two different techniques used have been compared to prove the accuracy of the results since hot-wire and LDV measurements are affected by different kind of problems. In the specific case a X-hot wire that suffer a velocity gradient has been used and its data have been treated with an a posteriori correction and then validated using the LDV measurements.

Descriptors: Fluid mechanics, rotating pipe flow, swirling jet, turbulence, hot-wire anemometry, LDV.

Parts of this work has been presented at:

The Swedish mechanics days, 11-13 June 2001 *Linköping, Sweden*

STEM/CECOST group conference, 5-7 November 2002 *Lund, Sweden*

TSFP3 conference, 25-27 June 2003 *Sendai, Japan*

Facciolo, L. Tillmark, N. & Talamelli, A. 2003 Experimental investigation of jets produced by rotating fully developed pipe flow, *TSFP3 conference proceedings*, 1217–1222.

STEM/CECOST group conference, 12-13 November 2003 *Gothenburg, Sweden*

Contents

CHAPTER 1

Introduction

1.1. Background

Swirling jets, where an azimuthal velocity is superimposed on the axial flow, are of importance in many technical and industrial applications. For instance, they are used in combustion systems both to enhance the forced convective cooling, to increase turbulent mixing of fuel with air and to stabilize the flame. Despite the importance of this type of flow and the large number of studies carried out in the past, there is still a lack of fundamental experimental data over a wider range of the Reynolds number and swirl number, to enhance the physical understanding of this type of flow as well as to assist in evaluating turbulence models and the development of CFD codes. In fact a large number of previous experimental investigations has used short stationary pipes with blades or vanes at the outlet to attain a swirling jet profile which contains traces of the swirl generator, hence perturbing the axial symmetry of the flow. In order to increase flow homogeneity and to decrease the influence of upstream disturbances, axi-symmetric contractions are sometimes used before the jet exit. However, in this way, swirled jets with top-hat exit profiles, characterized by thin mixing layers, are obtained. These type of jets may differ significantly from several industrial applications where fully developed pipe flow may better represent the real boundary conditions.

This thesis reports measurements and analysis both of the flow field in a fully developed rotating pipe as well as the resulting flow field of the emanating jet. This work is part of a larger project aimed at the studying of the effects of the impingement of a rotating fully developed jets on a flat plate, positioned relatively close to the pipe exit. For this reason the present experimental study is limited to the analysis of the initial near-exit and intermediate or transitional region

1.2. Equations

We will here first give the Navier-Stokes equations in cylindrical coordinates, and thereafter use Reynolds' decomposition to obtain the equations for the mean flow. When studying rotating flows it is possible to either use an inertial frame (laboratory fixed) or a rotating frame. In the first choice the rotation is felt through the boundary conditions, in the second the rotation is taken into account by adding body forces due to centrifugal and Coriolis effects.

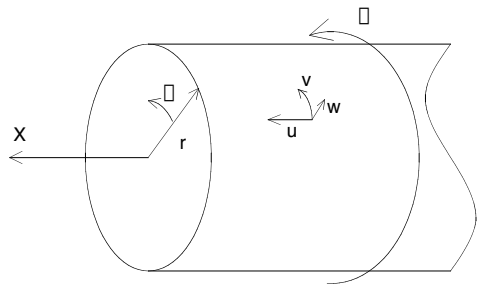

FIGURE 1.1. Coordinate system.

We write the equations in a general form in cylindrical coordinates such that both approaches will be possible. We denote the radial, azimuthal and axial directions with (r, θ, x) and the respective velocity components with (w, v, u), respectively. In the following we assume that the rotation is along the axial direction (in the laboratory frame the rotation vector can hence be written $\overline{\omega} = \omega \overline{e}_x$). Furthermore we assume that the flow is incompressible, i.e. the density ρ is constant as well as the temperature. As a consequence also the kinematic viscosity (ν) is constant. With these assumptions the conservation equation of mass (continuity equation) becomes

$$\frac{\partial w}{\partial r} + \frac{w}{r} + \frac{1}{r}\frac{\partial v}{\partial \theta} + \frac{\partial u}{\partial x} = 0 \tag{1.1}$$

whereas the conservation of momentum (Navier-Stokes equations) can be written

$$\begin{aligned} \frac{\partial w}{\partial t} + w\frac{\partial w}{\partial r} + \frac{v}{r}\frac{\partial w}{\partial \theta} + u\frac{\partial w}{\partial x} - \frac{v^2}{r} = \\ -\frac{1}{\rho}\frac{\partial p}{\partial r} + \nu\left(\frac{\partial^2 w}{\partial r^2} + \frac{1}{r}\frac{\partial w}{\partial r} - \frac{w}{r^2} + \frac{1}{r^2}\frac{\partial^2 w}{\partial \theta^2} + \frac{\partial^2 w}{\partial x^2} - \frac{2}{r^2}\frac{\partial v}{\partial \theta}\right) - 2\omega v \end{aligned} \tag{1.2}$$

$$\begin{aligned} \frac{\partial v}{\partial t} + w\frac{\partial v}{\partial r} + \frac{vw}{r} + \frac{v}{r}\frac{\partial v}{\partial \theta} + u\frac{\partial v}{\partial x} = \\ -\frac{1}{\rho r}\frac{\partial p}{\partial \theta} + \nu\left(\frac{\partial^2 v}{\partial r^2} + \frac{1}{r}\frac{\partial v}{\partial r} - \frac{v}{r^2} + \frac{1}{r^2}\frac{\partial^2 v}{\partial \theta^2} + \frac{\partial^2 v}{\partial x^2} + \frac{2}{r^2}\frac{\partial w}{\partial \theta}\right) + 2\omega w \end{aligned} \tag{1.3}$$

$$\begin{aligned} \frac{\partial u}{\partial t} + w\frac{\partial u}{\partial r} + \frac{v}{r}\frac{\partial u}{\partial \theta} + u\frac{\partial u}{\partial x} = \\ -\frac{1}{\rho}\frac{\partial p}{\partial x} + \nu\left(\frac{\partial^2 u}{\partial r^2} + \frac{1}{r}\frac{\partial u}{\partial r} + \frac{1}{r^2}\frac{\partial^2 u}{\partial \theta^2} + \frac{\partial^2 u}{\partial x^2}\right) \end{aligned} \tag{1.4}$$

where the Coriolis term is zero in the inertial (laboratory fixed) coordinate system. We proceed now with the Reynolds' decomposition

$$\begin{aligned} w &= W + w' \\ v &= V + v' \\ u &= U + u' \\ p &= P + p' \end{aligned}$$

where capital letters denote mean quantities and primed variables are fluctuating variables. Putting the decomposition into eqs. (1.1)–(1.4) and assuming that the mean flow is steady and axisymmetric, i.e.

$$\frac{\partial}{\partial t} = 0, \qquad \frac{\partial}{\partial \theta} = 0. \tag{1.5}$$

we obtain for the Reynolds averaged continuity equation

$$\frac{\partial W}{\partial r} + \frac{W}{r} + \frac{\partial U}{\partial x} = 0 \tag{1.6}$$

whereas the Reynolds averaged Navier-Stokes equations become (in the following we are skipping the prime on fluctuating components)

$$\frac{1}{\rho}\frac{\partial P}{\partial r} = -\frac{\partial}{\partial r}\overline{w^2} + \frac{1}{r}\left(V^2 + \overline{v^2} - \overline{w^2}\right) \tag{1.7}$$

$$U\frac{\partial V}{\partial x} + W\frac{\partial V}{\partial r} + \frac{VW}{r} = -\frac{1}{r^2}\frac{\partial}{\partial r}\left(r^2\overline{vw}\right) + \frac{1}{r^2}\frac{\partial}{\partial r}\left[\nu r^3\frac{\partial}{\partial r}\left(\frac{V}{r}\right)\right] \tag{1.8}$$

$$U\frac{\partial U}{\partial x} + W\frac{\partial U}{\partial r} = -\frac{1}{\rho}\frac{\partial P}{\partial x} - \frac{1}{r}\frac{\partial}{\partial r}\left(r\overline{uw}\right) - \frac{\partial}{\partial x}\overline{u^2} + \frac{1}{r}\frac{\partial}{\partial r}\left(\nu r\frac{\partial U}{\partial r}\right) \tag{1.9}$$

1.2.1. *Specializing to rotating pipe flow*

For a fully developed turbulent axially rotating pipe flow it is possible to simplify the equations significantly. First we must state the boundary conditions on the pipe wall which in the laboratory fixed coordinate system are:

$$W(R) = 0, \quad V(R) = V_w, \quad U(R) = 0, \tag{1.10}$$

where $V_w = \omega R$ is the velocity of the pipe wall. Due to symmetry the following conditions have to apply on the pipe axis

$$W(0) = 0, \quad V(0) = 0, \quad \frac{\partial U}{\partial r}(0) = 0 \tag{1.11}$$

For the fully developed case there is no streamwise variation of the mean quantities (except for the pressure) which immediately gives from the continuity equation (1.6) that $W = 0$ for all r.

Equation (1.8) can now be rewritten as

$$\nu\left(\frac{d^2V}{dr^2} + \frac{1}{r}\frac{dV}{dr} - \frac{V}{r^2}\right) = \frac{d}{dr}(\overline{vw}) + 2\frac{\overline{vw}}{r} \tag{1.12}$$

Equation (1.12) can be integrated twice, first from 0 to r, and thereafter from r to R (using the boundary conditions) to give (Wallin & Johansson 2000)

$$V(r) = V_w\frac{r}{R} - \frac{r}{\nu}\int_r^R \overline{vw}\frac{dr}{r} \tag{1.13}$$

The first term on the right hand side gives the solid body rotation whereas the second term gives a contribution from the Reynolds stress $\overline{vw}$ which means that if $\overline{vw} \neq 0$ the turbulence gives rise to a deviation from the solid body rotation. Also eq. (1.9) can be substantially simplified giving

$$0 = u_\tau^2\frac{r}{R} - \overline{uw} + \nu\frac{dU}{dr} \tag{1.14}$$

where u_τ is the friction velocity determined from the streamwise velocity gradient at the pipe wall (or equivalently the pressure drop along the pipe).

So far we have discussed the equations of motion in their dimensional form. However they can all be written in non-dimensional form by using only two non-dimensional numbers, namely the Reynolds number

$$Re = \frac{U_b D}{\nu} \tag{1.15}$$

and the swirl number

$$S = \frac{V_w}{U_b} \tag{1.16}$$

where U_b is the bulk velocity in the pipe. For instance eq. (1.13) can be written as

$$\frac{V(r)}{V_w} = \frac{r}{R}\left(1 - \frac{Re}{2S}\int_r^R \frac{\overline{vw}}{U_b^2}\frac{dr}{r}\right) \tag{1.17}$$

1.2.2. *Specializing to swirling jet flow*

For the turbulent axisymmetric jet flow we preserve the condition of symmetry at the centreline (r=0) and add the boundary conditions at infinity (r=∞):

$$U = 0, \quad V = 0, \quad W = 0, \quad \frac{\partial}{\partial r} = 0 \tag{1.18}$$

From the Reynolds averaged Navier-Stokes equations, multiplying the axial component (eq. 1.9) and the radial component (eq. 1.7) respectively by r and by r^2, then integrating between $r = 0$ and $r = \infty$ and applying the boundary conditions (1.18), we obtain (Chigier & Chervinsky 1967):

$$\frac{d}{dx}\int_0^\infty r[(P - P_\infty) + \rho(U^2 + \overline{u^2})]dr = 0 \tag{1.19}$$

$$\int_0^\infty r(P - P_\infty)dr = -\frac{1}{2}\rho\int_0^\infty r(V^2 + \overline{v^2} + \overline{w^2})dr \tag{1.20}$$

From the above equations, considering that the squared fluctuating velocity components are negligible with respect to the squared mean components, we get the conservation of the flux of the axial momentum

$$\frac{d}{dx}\left(2\pi\rho\int_0^\infty r(U^2 - \frac{1}{2}V^2)dr\right) = \frac{d}{dx}G_x = 0 \tag{1.21}$$

In the same way, starting from the azimuthal component (eq. 1.8) of the Reynolds averaged Navier-Stokes equations , multiplying and integrating it we get the angular momentum

$$\frac{d}{dx}\left(2\pi\rho\int_0^\infty r^2UVdr\right) = \frac{d}{dx}G_\theta = 0 \tag{1.22}$$

By using the above quantities it is possible to characterize the swirling flow with an integral swirl number:

$$S_{\theta x} = \frac{G_\theta}{G_x R}. \tag{1.23}$$

1.2.3. *Vortex Models*

The distribution of the azimuthal velocity in a real jet is mainly due to the method used to generate the swirl. From a mathematical point of view, it is possible to create models to properly approximate the behaviour of the flow field.

A Rankine vortex represents a simply model for rotating flow (figure 1.2a). It displays a solid body rotation core followed by a r^{-1} decay in the radial direction. In application to a swirling jet, it is worth to note that the model does not take in account the finite thickness of the shear layer region at $r = R$ where the curve has a singularity.

$$V = \Lambda r, \quad 0 \leqslant r \leqslant R \tag{1.24}$$

$$V = \frac{\Lambda R^2}{r} \tag{1.25}$$

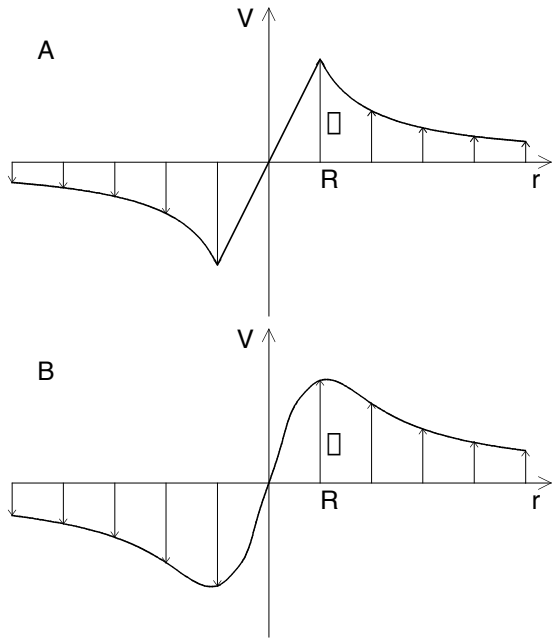

FIGURE 1.2. a) Rankine vortex, b) Batchelor vortex.

A more suitable model for developed swirling flows is the Batchelor vortex (figure 1.2b). The azimuthal velocity field is described via a similarity solution applied to wakes and jets in the far field. In a non-dimensional formulation the velocity has a maximum ($V = \Lambda$) for $r = 1.121$.

$$V = \frac{\Lambda}{0.638} \frac{1 - e^{-r^2}}{r} \tag{1.26}$$

CHAPTER 2

Review of rotating pipe flow studies

The physics of rotating pipe flow is a challenge for experimental, theoretical, modelling and simulation studies despite its conceptual simplicity. A few experimental studies have been undertaken and there are also some direct numerical simulation studies available. However a large number of studies using rotating turbulent pipe flow as a test case for modelling can be found in the literature.

First it should be clearly stated that the effect on rotation on pipe flow is quite different depending on whether the flow is laminar or turbulent. In the laminar case rotation has a destabilizing effect and the critical Reynolds number is as low as 83 for linearized disturbances. Turbulent pipe flow on the other hand, is stabilized by rotation and for instance the pressure drop along the pipe decreases with increasing rotation rate. It should also be mentioned that in the laminar case the fluid approaches solid body rotation at some distance downstream the inlet, whereas for turbulent flow this is not the case. We will first give a brief review regarding the present state of results for rotating laminar pipe flow and then discuss the turbulent case, describing first the experimental work as well as DNS work, and finally discuss some of the modelling attempts.

2.1. Stability of laminar rotating pipe flow

There have been several studies regarding the stability of rotating pipe flow. For instance Howard & Gupta (1962) gave an inviscid stability criterion for rotating pipe flow which is valid for axisymmetric disturbances. More thorough studies were made by Pedley (1968, 1969) who investigated the linear stability of rotating pipe flow both through an inviscid as well as a viscous analysis. He showed that in the limit of high rotation rates the critical Reynolds number became as low as 83 and remarked that this may be surprising since both a fluid undergoing solid body rotation as well as the pipe flow itself are stable, but gave no physical interpretation of the results.

Toplosky & Akylas (1988) expanded on the previous results into the non-linear regime and showed that the instability was supercritical and that it would take the form of helical waves. Recently Barnes & Kerswell (2000) confirmed these results and found that the helical waves may become unstable to three dimensional travelling waves. These studies also concluded that the disturbances could not be traced back to the non-rotating case, thereby they are not the source for transition in non-rotating pipe flow.

Experimental work for this case has been limited to a few studies. There are of course experimental problems to set up this flow since both the parabolic Poisueille profile as well as the solid body rotation will take some downstream distance from the inlet to become fully established. In the experiments by Nagib *et al.* (1971) a fairly short pipe was used ($L/D \approx 23$ so the parabolic profile was not fully developed), however the rotation was obtained by the letting the fluid (water) pass through a porous material inside the rotating pipe, thereby efficiently bringing the fluid into rotation. They observed, from flow visualization and hot-film measurements, that the transitional Reynolds number decreased from 2500 to 900 when S increased from 0 to 3. A more recent study by Imao *et al.* (1992) shows details of the instabilities through both LDV-measurements and flow visualizations. They also demonstrate that the instability takes the form of spiral waves.

There are a few attempts to pinpoint the physical mechanism behind the instability in terms of a Rayleigh criterion or centrifugal instability, but as pointed out by Maslowe (1974) the theoretical analysis has so far not been able to shed light on this mechanism. To this end we will only point out a similarity of the basic flow field as seen in a non-rotating inertial frame with that giving rise to cross flow instabilities on a rotating disc or a swept wing.

2.2. Turbulent rotating pipe flow

2.2.1. *Experimental results*

The first experimental study of rotating pipe flow is probably that of White (1964) who showed that the pressure drop in the turbulent regime decreased with increasing rotation. He also did some flow visualization both illustrating the destabilization in the laminar case and the stabilization in the turbulent one.

Murakami & Kikuyama (1980) did their experiments in a water flow facility where the pipe diameter was 32 mm. They measured both the pressure drop as well as mean velocity profiles. For the pressure drop measurements they presented data for Reynolds numbers in the range $10^4 - 10^5$ and for rotation rates up to $S = 3$. The pressure tappings were placed in the stationary pipes upstream and downstream of the rotating section and the length of the rotating section could be varied by using interchangeable pipes of various lengths. The mean velocity in the streamwise and azimuthal directions were measured with a three hole Pitot tube which was inserted through a stationary part of 5 mm length which could be placed at different positions from the inlet of the rotating pipe.

They found that when the pipe length is larger than 100 diameters, the ratio between the loss coefficient for a rotating pipe and a non-rotating smooth pipe is governed only by the rate of rotation S. Beyond $S = 1.2$ the observed suppression of turbulence is saturated and the ratio of the loss coefficients remains unaltered. In the Reynolds range considered during the experiment

($10^4 < Re < 2 \cdot 10^5$), the axial velocity profiles gradually change in the downstream direction to become less full, i.e. the centreline velocity increases and the velocity gradient at the wall decreases. For $x/D > 120$ the velocity profile results were found to be approximately independent of the axial distance from the inlet. The change of the velocity profile is more accentuated with increasing S and tends towards the parabolic shape of a laminar flow. However the azimuthal velocity profiles at this position does not show solid body rotation, instead it has a shape which is nearly parabolic, $V/V_w = (r/R)^2$.

LDV-measurements were made by Kikuyama *et al.* (1983) who expanded the measurements by Murakami & Kikuyama (1980) to other pipe diameters (5 and 20 mm) and also presented velocity measurements taken by an LDV system. These results confirm the previous results that the mean flow tends to a parbolic profile when rotation is increased and that the azimuthal flow also becomes parabolic. Unfortunately no data on the turbulence fluctuations were presented. Similarily the experiments by Reich & Beer (1989) in the range $5000 < Re < 50000$ and S up to 5, showed mean profiles of both the streamwise and azimuthal directions obtained with a three-hole pressure probe which are in accordance with the earlier results. Also in this case only mean velocity data were obtained.

The LDV measurements by Imao *et al.* (1996) on the other hand supplied the first measurements of turbulence fluctuations and presented measured distributions on five of the Reynolds stresses as well as the mean profiles at $Re = 20000$. The measurements were made in water in a 30 mm diameter pipe at $120D$ dowstream the inlet. They also presented pressure drop measurements showing the decrease of the friction factor with increasing S. Their measurements confirmed the previously observed change in the streamwise velocity as well as the parabolic shape of the azimuthal velocity. If the normal stresses were normalized with the bulk velocity there was only a slight decrease with increasing rotation. The change in $\overline{uw}$ was on the other hand much more dramatic if normalized with the bulk velocity, but would more or less collapse if normalized with the friction velocity. $\overline{uv}$ is for the non-rotating case equal to zero due to symmetry, but was seen to become negative with rotation. A plausible explanation for this behaviour is that the normal velocity increases with r whereas the opposite is true for the streamwise velocity. A fluctuation that gives a radial displacement of a fluid element which keeps its momentum would hence give $u > 0$ and $v < 0$ (or vice versa) which would mean that the fluctuations would become negatively correlated.

2.2.2. *Numerical simulations*

Although experimental studies of rotating pipe flow have been performed since long, direct numerical simulations (DNS) and large eddy simulations (LES) of turbulent pipe flow have been reported only during the last decade. The first results from large eddy simulations seem to be reported in the doctoral thesis of Eggels (1994). He did a simulation at Re=59500 and S=0.71. He found

that the streamwise mean velocity increased in the centre of the pipe and a subsequent decrease at the wall, and hence a smaller friction coefficient. The azimuthal velocity showed the expected near-parabolic shape and the turbulent decreased, especially close to the pipe walls. The largest decrease was seen in the streamwise component.

Orlandi & Fatica (1997) on the other hand performed a DNS at $Re = 5000$ for four values of S, namely 0, 0.5, 1.0 and 2.0. They presented data for both the mean flow velocity and all six Reynolds stresses as well as some instantaneous flow field data. Orlandi (1997) used this data base to further evaluate various turbulent quantities. Later Orlandi & Ebstein (2000) made simulations at approximately the same Reynolds number but extended the rotation rates up to $N = 10$. In that case they especially focussed on presenting the turbulent budgets for different S.

The data of Orlandi & Fatica (1997) and Orlandi & Ebstein (2000) show that the friction factor decreases with about 15% when S is increased from 0 to 2. However for $S = 5$ the friction factor increase again and at $S = 10$ it is actually higher than for the non-rotating case. The streamwise velocity profiles show a similar behaviour as in the experiments described in section 2.2.1, the centreline velocity increases with S and the profile becomes less full. When scaling these profiles with the bulk velocity it has been noted that, keeping the Reynolds number constant and varying S, all the profiles collapse almost at the same value $U/U_b = 1.14$ at $r/R \approx 0.6$ presenting a good agreement with experimental data (the difference is referred to the effect of the entrance conditions). The azimuthal profile also shows the expected parabolic behaviour, except close to the wall, although there is a slight variation with S.

The results for the normal Reynolds stress components show that rotation gives a reduction of the near wall maximum in the streamwise component and a slight increase in the other two, especially in the central region of the pipe.

In a non-rotating pipe the only resulting shear stress is $\overline{uw}$. The simulation data show that when a rotation is introduced it is slightly reduced and there is an increase in $\overline{uv}$ and $\overline{vw}$ instead. The distribution of $\overline{vw}$ can be shown (see eq. 1.17) to be directly coupled to the azimuthal mean flow distribution and scales with S/Re and the calculated distributions show the expected shape. However the $\overline{uv}$ distribution has a strange behaviour for $S \geq 1$, with oscillations along the pipe radius. Orlandi & Fatica (1997) explain this with the large scale structures in the central region of the pipe for high S which means that the averaging time has to be increased to obtain stable distributions.

A recent DNS study was made by Satake & Kunugi (2002) at a similar Reynolds number and values of S of 0.5, 1.0, 2.0 and 3.0. In that study a uniform heat flux was introduced at the wall and temperature distributions were also calculated. Their data show a monotonous decrease of the friction factor with increasing S. In addition to mean flow distributions and Reynolds stresses they present detailed turbulent budgets which are similar to those of Orlandi & Ebstein (2000), as well as similar profiles for the temperature

fluctuations. It can be noted that their $\overline{uv}$-data also show oscillations in the same way as the data of Orlandi & Fatica (1997) for high S.

Finally two recent LES studies have also been published (Yang (2000), Feiz *et al.* (2003)) which for suitable subgrid scale models to a large extent show good agreement with the DNS results.

2.2.3. *Theoretical and numerical modelling*

In a rotating pipe flow the rotation affects both the mean flow as well as the turbulent stresses. To some extent the stabilizing effect of the rotation can be taken into account in the models by introducing a correction in terms of a Richardson number. For instance Kikuyama *et al.* (1983) modelled the turbulence using Prandtls mixing length theory where the mixing length was modified, such that the stabilizing influence of rotation was taken into account through a Richardson number which involves the azimuthal velocity. Such an approach was first suggested by Bradshaw (1969), however in order to use this Kikuyama *et al.* had to assume that the azimuthal velocity had the experimentally observed parabolic shape. In their calculations they were able to obtain the observed change in the streamwise velocity distribution as well as the friction factor although with this approach the azimuthal velocity distribution is an input to the model and the modelling is therefore of somewhat limited value. Also the work by Weigand & Beer (1994) follows similar lines.

On the other hand it has been shown that the standard K-ϵ model cannot model even the streamwise mean flow correctly. For instance the results of Hirai, Takagi & Matsumoto (1988) show that it does not predict the changes in the streamwise velocity profile when $S \neq 0$ and the resulting azimuthal velocity becomes linear, i.e. the model predicts a solid body rotation of the flow. This is also true when the model is modified using a Richardson number to take into account the stabilizing effect of rotation. This issue has been thoroughly discussed by Speziale, Younis & Berger (2000).

Hirai *et al.* (1988) employed a Reynolds stress transport equation model which was shown to be able to give the correct tendency of the experimentally measured axial velocity profile as well as the tendency of the friction factor to decrease with increasing swirl. The laminarisation phenomenon is explained by the reduction of the turbulent momentum flux $\rho\overline{uw}$ due to the swirl, mainly caused by the negative production term $\overline{uv}V/r$ in the transport equation of $\overline{uw}$. Other attempts giving similar results using Reynolds stress transport models to calculate rotating turbulent pipe flow have been made by Malin & Younis (1997), Rinck & Beer (1998) and Kurbatskii & Poroseva (1999).

Both Speziale *et al.* (2000) and Wallin & Johansson (2000) developed algebraic Reynolds stress models which were applied to rotating pipe flow. They used different approaches to the modelling, for instance Speziale *et al.* worked in the rotating system, taking the rotation into account through the Coriolis force, whereas Wallin & Johansson used the inertial system (laboratory fixed). In that case the rotation effects come in through the rotating pipe wall (i.e.

through the boundary conditions). In both cases their models were able to qualitatively show the main features of rotation, namely the change in the streamwise velocity with S and the deviation from the solid body rotation of the azimuthal velocity distribution.

Finally the theoretical modelling of turbulent flows by Oberlack (1999, 2001) should be mentioned. He has, through a Lie group appoach to the Reynolds averaged Navier-Stokes equations, been able to derive new scaling laws for various turbulent flows, among them rotating pipe flow. Of particular interest for the present work is that Oberlack (1999) proposes certain scaling laws that can be checked against experiments. For instance the theory gives that the azimuthal mean velocity can be written as

$$\frac{V}{V_w} = \zeta \left(\frac{r}{R}\right)^{\psi} \tag{2.1}$$

which with $\zeta = 1$ and $\psi = 2$ corresponds to the parabolic velocity distribution. Furthermore the theory suggests a scaling law for the axial mean velocity which is

$$\frac{U_c - U}{u_\tau} = \chi \left(\frac{V_w}{u_\tau}\right) \left(\frac{r}{R}\right)^{\psi} \tag{2.2}$$

where χ is a function of the velocity ratio between the rotational speed of the pipe and the friction velocity. Note that the value of the exponent ψ in eqs. (2.1) and (2.2) is the same. A logarithmic law in the radial coordinate is also suggested from the theory, such that

$$\frac{U}{V_w} = \lambda \log\left(\frac{r}{R}\right) + \omega \tag{2.3}$$

This scaling law was checked against the data of Orlandi & Fatica (1997). Only data for one swirl number was shown (S=2), but a logarithmic region was found for $0.5 \leq r/R \leq 0.8$ with λ=–1.0. A final proposition from the theory is that there is one point where the mean axial velocity is independent of the Reynolds number. The data suggest that this fixed point is $r_{fix} = 0.75R$ and that the velocity is $U(r_{fix}) = U_b$. In the present study we will compare our experimental data with the predictions of Oberlack (1999).

CHAPTER 3

Review of axisymmetric jet

Jet flows with different geometries and boundary conditions have been widely investigated both experimentally and theoretically. The importance of this type of shear flow is related to numerous industrial applications (e.g. combustion, jet propulsion and cooling systems). This chapter contains an overview of work on swirling jet flows. In order to assess the main features and effects due to the presence of the rotational motion of the flow, a brief review concerning the main characteristics of axisymmetric non-swirling jets is also included.

3.1. The axisymmetric jet

An axisymmetric jet (see figure 3.1) is produced when fluid is ejected from a circular orifice into an external ambient fluid, which can be either at rest or co-flowing. Here we assume that the jet fluid and the ambient fluid are the same. At the nozzle exit, the high velocity jet generates a thin axisymmetric circular shear layer. The shear layer is rapidly subjected to a Kelvin-Helmoltz instability process (due to the presence of an inflectional point in the mean streamwise velocity distribution) and vortical structures are formed. Moving downstream the shear layer spreads in the radial direction both outwards and towards the centreline. The shear layer reaches the jet axis at a distance of approximately 4–5 diameters from the exit. The region inside the axisymmetric shear layer, characterized by an unchanged axial velocity, is called the jet "potential" core. The process described above is similar both for laminar and turbulent jet flows.

Further downstream, in the intermediate region of the jet, the different eddy structures interact in a non-linear behaviour engulfing fluid from the external environment and eventually collapse leaving the jet fully turbulent.

In the fully turbulent region, i.e. after approximately 20 diameters downstream the jet exit, the mean velocity profiles exhibit a self-preservation behaviour where the mean axial centreline velocity decays with the inverse of the distance. However, the turbulence intensity profiles require a much longer distance before reaching the self-preservation state, especially for the radial and tangential fluctuations. This is due to the fact that the energy is directly transferred from the mean flow to the streamwise fluctuations whereas energy to the other two components is transferred from the streamwise turbulence through the pressure-strain terms. Only after about 50–70 diameters the axisymmetric jet can be considered as truly self-preserving. For a review of turbulent jets

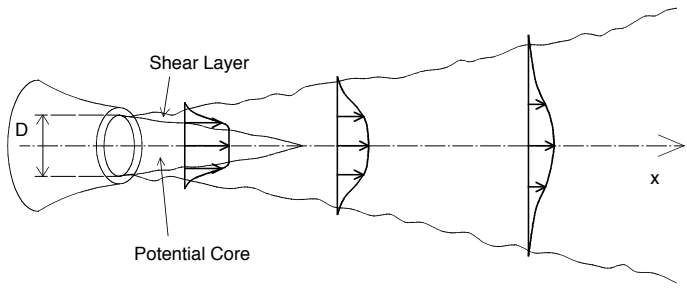

FIGURE 3.1. Schematic of the development of an axisymmetric jet.

the reader is referred to the monograph of Abramovich (1963) or to the more recent review article by Thomas (1991).

3.1.1. *The initial region*

The near field of an axisymmetric jet is dominated by the inviscid inflectional instability mechanism that amplifies upstream disturbances and generates large-scale vortical structures in the shear layer. The shape and characteristics of the structures depend on the type of the disturbances. In the initial region of naturally evolving jets it appears that axisymmetric disturbances are mostly amplified, giving rise to quasi-periodically spaced axisymmetric rings of concentrated vorticity.

Amplification factors and phase velocities depend on the main characteristics of the shear layer, such as the mean velocity profile and the thickness of the boundary layer at the jet exit. In particular, the frequency of the most amplified disturbances scales with the shear layer thickness and with the local velocity profile, but does not depend on the jet diameter (shear layer mode). Indeed Michalke (1984) in his review, shows that the instability at the exit of an axisymmetric jet can be treated as a planar shear layer instability if the ratio between the radius and the shear layer thickness is larger than 50. In such a case the instability mode behaves as if it is two-dimensional. Further downstream, the shear layer thickness of course increases and when it becomes of the same order as the jet radius, the curvature cannot be neglected anymore.

Moving downstream the structures start to merge and to interact creating even larger structures. This mechanism is the one by which the memory of the initial stability is gradually lost. At the end of the potential core the

appropriate length scale of the instability becomes the jet diameter. The passage frequency of the large-scale structures in this region is referred as the preferred mode or jet column mode. This mode can be described by means of a non-dimensional frequency, $St = fD/U$ (Strouhal number), where f is the frequency, D the jet diameter and U the jet exit velocity. In the different experiments in the literature a quite broad range ($0.25 < St < 0.85$) of the jet column mode has been found. This disagreement between different experiments may be explained with the extreme sensitivity of the jet instability to the upstream noise coming from the experimental set-up. Indeed, with this type of instability a wide range of frequencies is highly amplified.

Finally, it must be stated that the shear layer mode and the jet column mode may not be perfectly decoupled. In fact, both hydrodynamics and acoustic feedback effects can be present (see e.g. Hussain (1986)). The time signal and eddy formation at the jet exit and in the intermediate region may be triggered by the feedback from the structures which evolve downstream. This feedback may also play an interesting role in sustaining self-excited excitation.

3.1.2. *The developed region*

In the intermediate region of the axisymmetric jet the large-scale coherent structures interact with each other. Merging, tearing or secondary instability phenomena are present. In this region, the structures are responsible for the bulk of the engulfment of ambient fluid with the consequent increasing of the entrainment activity (Komori & Ueda (1985), Liepmann & Gharib (1992)). The helical instability has a growing importance as the flow approaches the end of the potential core and becomes dominant in the fully developed region. Increasing the axial distance, the helical structures, with right handed and left handed modes of equal probability, move radially outwards (Komori & Ueda 1985) giving, together with local ejection of turbulent fluid and bulk entrainment of ambient fluid, a great contribution to the jet spreading. At large distances from the jet exit (more than 20 diameters) the jet width increases linearly with the streamwise coordinate while the centreline velocity decays as x^{-1}. In this region the external periodic excitation useful to describe the large-scale structure behaviour in the near exit region is of little use. Moreover, flow visualization cannot help in studying this region since the marker is highly dispersed due to the small-scale diffusivity. However, some researchers still try to study the coherent structures even far away from the jet exit. In this case only a sort of statistical coherent structure is depicted and characterized.

3.2. The axisymmetric swirling jet

The near field of a non-swirling jet is mainly driven by instabilities or turbulent mixing and the pressure plays a minor role. However, when a tangential velocity component is superimposed on the axial one in a circular jet, both radial and axial pressure gradients are generated. These gradients may significantly

influence the flow changing the geometry, the evolution and the interactions between the vortical structures.

For swirling jets different flow regimes may be identified depending on the degree of swirl present in the jet. For low swirl numbers (i.e. when the maximum tangential velocity is of the order of 50% or less of the axial centreline velocity) the jet behaves in a similar way as for the non-swirling case, even though some modification in the mean and fluctuating velocity distributions, jet width or spreading are present. Some changes in the dynamics of the large vortical structures are also present. However, when the swirl becomes strong (i.e. when the tangential velocity becomes larger than the axial velocity), the adverse axial pressure may be sufficiently large to establish a reversed flow on the jet axis and a complete different scenario is present. This is usually called the vortex breakdown regime. In between these two regimes an intermediate regime is established. The behaviour of the jet in this case is the results of complicated interactions between modes, which are typical of axisymmetric jets and rotating flows.

3.2.1. *Definition of the swirl number*

In general, the Reynolds number for an axisymmetric jet is based on the diameter of the nozzle and on the axial velocity at the centreline or the bulk velocity. On the other hand the definition of the swirl number varies between different studies. A common way is to express the swirl number as the ratio between the fluxes of the tangential and axial momentum ($S_{\theta x}$, see eq. 1.23). However, such a measure means that the velocity profiles of both the streamwise and azimuthal velocities need to be measured accurately to allow the integration across the jet orifice. This is in some cases not possible nor practical and other measures have been suggested by various researchers.

Chigier & Chervinsky (1967) proposed that $S_{\theta x}$ could be determined as the ratio between the azimuthal velocity maximum and the axial velocity maximum at the orifice, whereas Billant *et al.* (1998) used a swirl number based on the ratio between the azimuthal velocity measured at half the radius of the nozzle and the centreline axial velocity at about one diameter downstream the jet outlet. It has also been shown (Farokhi *et al.* (1988)) that for some cases the measure $S_{\theta x}$ is inappropriate to characterize the vortex breakdown since two jets with different velocity profiles can still have the same swirl number but different development of the flow field. In the present work, however, there exist natural outer parameters that can be used to determine a swirl number, namely as the ratio between the azimuthal velocity at the pipe wall (maximum azimuthal velocity) and the mean bulk axial velocity (see eq. 1.16).

3.2.2. *Swirl generation techniques*

There are many reported experiments on swirling jets, however the methods to generate the swirl differ, which also means that the outlet velocity distribution

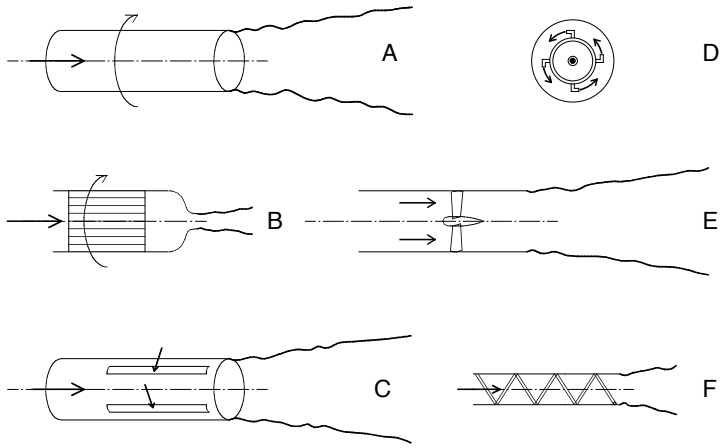

FIGURE 3.2. Schematic of six different methods to genearte a swirling jet. A) Rotating pipe, B) Rotating honeycomb, C) Tangential slots, D) Tangential nozzles, E) Deflecting vanes, F) Coil insert.

will vary between different experiments. In the following we will describe some of these methods which also are sketched in figure 3.2.

3.2.2.1. *Rotating methods*

In the present work we use a long, axially rotating pipe to estabish the swirling flow, which is the same principle as that used by Rose (1962) and Pratte & Keffer (1972). Rose (1962) used a pipe with an L/D =100 and assumed that the flow was in solid body rotation at the outlet, whereas Pratte & Keffer (1972) used a somewhat shorter pipe in their experiment. In that case they used a flow divider at the inlet which brought an azimuthal component to the flow. From the foregoing section we are now aware that only a laminar pipe flow will have a solid body rotation, whereas a turbulent rotating pipe flow will not, even if the pipe was infinitely long. However, if the pipe is sufficiently long, this is probably the one method for which the resulting flow is most independent of the the individual set-up.

Komori & Ueda (1985) adopted a similar technique adding a convergent nozzle to the rotating pipe. However in this case the azimuthal and axial velocity components will be affected differently by the contraction. From an inviscid analysis one obtains that the axial velocity will increase in proportion to the contraction ratio (CR) whereas the azimuthal only as the square root

of CR. In reality also the detailed geometry of the contraction will play a role and therefore different set-ups will give different outlet profiles.

Billant *et al.* (1998) and Loiseleux & Chomaz (2003) used a motor driven, rotating honeycomb before a contraction nozzle. In their case the Reynolds number is low and the honeycomb ensures a laminar flow with solid body rotation. However when the flow goes through the contraction it is distorted and the axial velocity becomes pointed at the centre and the flow does not seem to be in solid body rotation.

3.2.2.2. *Secondary flow injection*

A different technique is to inject fluid tangetially in the pipe section. Chigier & Chervinsky (1967) utilized tangential slots in a mixing chamber set before the nozzle where a tangential flow was supplied to the main axial flow. The regulation of the flow field was made by varying the relative quantities of axial and tangential air.

A similar principle was used by Farokhi *et al.* (1988) who instead introduced the flow inside the pipe through concentric manifold rings and elbow nozzles upstream a bell-mouth section driving the air to the nozzle exit. Also here the swirl rate can be set by controlling the proportion of axial to tangential air.

3.2.2.3. *Passive methods*

A passive method to introduce swirl is through a swirl generator with annular vanes that deflect the flow before the nozzle exit (see e.g. Sislian & Cusworth (1986), Panda & McLaughlin (1994) and Lilley (1999)). In this case the ratio between the axial and the swirl components depends mainly on the tilting angle of the blades.

Another possibility is to use a coil insert mounted at the wall to impose the swirl component (see for instance Rahai & Wong (2001)). Also in this case the flow depends on the geometrical parameters of the coil.

3.2.3. *Swirling jet instability*

The spatial and temporal instability of a swirling jet has been investigated both experimentally and theoretically. Several analytical investigations have been performed in order to find the linear stability of different combination of axial velocity profiles and a rotational motion. In this type of flow the Kelvin–Helmoltz and the centrifugal instabilities may be present simultaneously since, in addition to the velocity gradient, the shear layer experiences the radial pressure gradient due to the azimuthal component of velocity.

Similarly to the Kelvin-Helmoltz instability criterion a criterion for the centrifugal instability can be introduced. The following relation gives necessary and sufficient condition for the onset of the axisymmetric mode:

$$\frac{d}{dr}(rV)^2 < 0 \tag{3.1}$$

This means that the circulation must decrease with increasing radial distance. Other criteria taken into account an axial flow both for axisymmetric and helical modes have also been proposed (see e.g. Leibovich & Stewartson (1983), Loiseleux & Chomaz (2003)).

Lessen *et al.* (1974) studied the temporal instability of a Batchelor vortex for different values of a swirl parameter related to the relative intensity of the axial and azimuthal velocities. Viscosity was also added in a following study (Lessen & Paillet (1974), see also Khorrami (1995), Mayer & Powell (1992)). However this model was not adequate to describe the instability of a swirling jet since the axisymmetric mode was found to be always stable.

A more realistic flow model was studied by Martin & Meiburg (1994), for which there is a jump both in the azimuthal and streamwsie velocity at the jet periphery. They concluded that a centrifugally stable jet may be destabilzed by Kelvin-Helmholtz waves which in their model originate from the jump in the azimuthal velocity. In another study Loiseleux *et al.* (1998) investigated the stability of a Rankine vortex with an added plug flow. In contrast to the Batchelor vortex this type of flow is unstable to axisymmetric disturbances. Moreover, the swirl breaks the symmetry between negative and positive helical modes, which is a typical characteristic of a non-swirling jet. In their work they also studied the absolute/convective nature of the instability.

Absolute instability in swirling flows has been analyzed by Lim & Redekopp (1998) and Michalke (1999). They showed that the tendency towards absolute instability is increased when the shear layer is centrifugally unstable.

An experimental study of the Kelvin-Helmoltz instability in a swirling jet was performed by Panda & McLaughlin (1994). Their analysis is concentrated to high swirl numbers (close to the breakdown) and they conclude that swirl tends to reduce the amplification of the unstable modes.

Loiseleux & Chomaz (2003) made a well-detailed experimental analysis on the instability of swirling jet and found three different flow regimes for swirl numbers below that for which vortex breakdown occurs. They used the same experimental set-up as that of Billant *et al.* (1998). For small swirl numbers the rotation does not affect the jet column mode and that case behaves similarly to the non-swirling case. As the swirl number increases the amplitude of this mode decreases and instead a helical mode grows. Moreover, a different secondary instability mechanism is set. Co-rotating streamwise vortices are formed in the braids, which connects the rings. In the intermediate swirl range these two instability mechanisms compete against each other. This scenario becomes more and more complicated when the swirl number is increased. Just before the breakdown strong interactions between azimuthal waves and ring vortices are observed.

Numerical studies concerning the analysis of non-linear axisymmetric and three-dimensional vorticity dynamics in a swirling jet model have been performed by Martin & Meiburg (1998). They used a vortex filament technique to perform a numerical simulation of the non-linear evolution of the flow, whereas

Hu *et al.* (2001) used DNS to study a temporally evolving swirling jet near the exit under axisymmetric and azimuthal disturbances.

3.2.4. *Studies of turbulent jets at moderate swirl numbers*

Most of the early analysis of swirling jets are based on experimental works, mainly focused on measuring mean profiles or turbulent transport properties, even though some theoretical works concerning laminar swirling jets are also reported in the literature. In one of these first investigations, Rose (1962) showed that even a weak swirl could radically change the character of the radial motion in the jet.

An early work by Chigier & Chervinsky (1967) shows that approximately at 10 diameters from the jet exit the influence of the rotation becomes small. An attempt to theoretically describe the flow based on the integration of the Reynolds equations is also shown. Good agreement is found giving the possibility to formulate semi-empirical equations, which, when calibrated with the experimental results, give the complete description of the mean velocity and pressure fields. However, the role of the initial conditions is not clear, viz. exit velocity profile, turbulence level, and status of the boundary layers before the jet exit.

In this period most of the experimental works (like for instance Pratte & Keffer (1972)) were devoted to the study of specific configuration of swirled jets. Nevertheless, some general conclusions could be assessed. For instance it was shown that the entrainment and the spreading was increasing with respect to the non-swirling jet.

Park & Shin (1993) showed experimentally that for swirl number less than 0.6 the entrainment is independent of the Reynolds number increasing non-linearly with the downstream region. For $S > 0.6$ the entrainment increases and becomes higher with Re probably due to a precessing vortex core phenomenon.

In order to find similarity in both mean and fluctuating components, Farokhi *et al.* (1988) showed that in the near field the mean velocity profiles strictly depend on the initial conditions. The size of the vortex core and the tangential velocity distribution seem to be the main controlling parameters. In a later study, Farokhi *et al.* (1992) considered the excitability of a swirling jet in the subsonic region. They found that periodic coherent vortices could be generated by plane-wave acoustic excitation. In contrast to non-swirling jets they found that vortex pairing is not an important mechanism for the spreading of a swirling jet.

In the presence of strong swirl, the large negative static pressure generated by the centrifugal forces may induce a reverse flow and the rapid entrainment in the region immediately after the jet exit ($x/D < 1$). Strong differences appear also in the fluctuating components. Komori & Ueda (1985) showed that the turbulent kinetic energy attains a maximum in this region, due to the rapid mixing. Conversely, in a weak swirling or non-swirling jet the turbulent mixing is weak in the potential core region and the turbulent kinetic energy

attains its maximum further downstream. Beyond the recirculating region the turbulence decays rapidly and becomes rather isotropic due to the strong mixing. More extensive measurements of highly swirling flows are made by Sislian & Cusworth (1986) and by Metha *et al.* (1991). They also show that the maximum turbulence is produced in the shear layer at the edge immediately after the exit.

More recently McIlwain & Pollard (2002) studied the interaction between coherent structures in a mildly swirling jet. Time-dependent evolution and the interaction of the structures are well documented.

3.2.5. *The vortex breakdown*

The vortex breakdown phenomenon has attracted considerable interest and Billant *et al.* (1998) give an up to date review of the literature on vortex breakdown in swirling jets. The vortex breakdown appears as an abrupt deceleration of the flow near the axis with the settling of a stagnation point generated by the axial increase of the pressure that is able to bring the axial velocity to zero. In experiments four different breakdown configurations have been observed: bubble, cone, asymmetric bubble and asymmetric cone. Here we will not go into any more detail since for the part of the the present work which deals with swirling jets ther swirl rate are below that for which vortex breakdown occurs.

CHAPTER 4

Experimental facility and setup

For the present study a new experimental facility has been designed and taken into operation at the Fluid physics laboratory of KTH Mechanics. The design philosophy has been to obtain a swirling jet flow with well defined characteristics which are independent of the specific geometry, i.e. the flow characteristics should not depend on the specific geomtry of swirl generators etc. To achieve this goal it was decided to use a long rotating pipe in order to obtain a fully developed turbulent pipe flow both with and without swirl, such that it would be independent of the inlet conditions. The Reynolds number of the study was decided to be of the order of $20 \cdot 10^3$ with possible variations of $\pm 50\%$. This means that the Reynolds number is high enough not to be influenced by transitional, intermittent structures. At the onset of the study the swirl number of interest was decided to be from zero (no rotation) up to 0.5.[1]

The length (L) of the pipe in terms of pipe diameters (L/D) is one of the crucial design parameters in order to obtain a fully developed flow. The relation between the Reynolds number (Re) and the swirl number (S) can be expressed as

$$S \cdot Re = \frac{\omega D^2}{2\nu}$$

Since we have for other reasons decided to use air as the flow medium, and hence the value of ν is fixed, the desirable Reynolds and swirl number ranges then set certain limits on the pipe diameter and pipe angular velocity. Both from lab space restrictions and the possibility to obtain pipes in one piece of good quality (in terms of roundness and surface quality) it was decided to use a pipe of six meter length with a diameter of 60 mm. This gives an L/D-ratio of 100 which was deemed sufficiently long to give a fully developed flow both with and without rotation if the incoming air has a rotational motion from which it then could establish its fully developed characteristics. The necessary rotational speed is about 13 revolutions per second in order to obtain a swirl number of 0.5 at $Re = 20 \cdot 10^3$.

[1] This range was later extended up to a swirl number of 1.5.

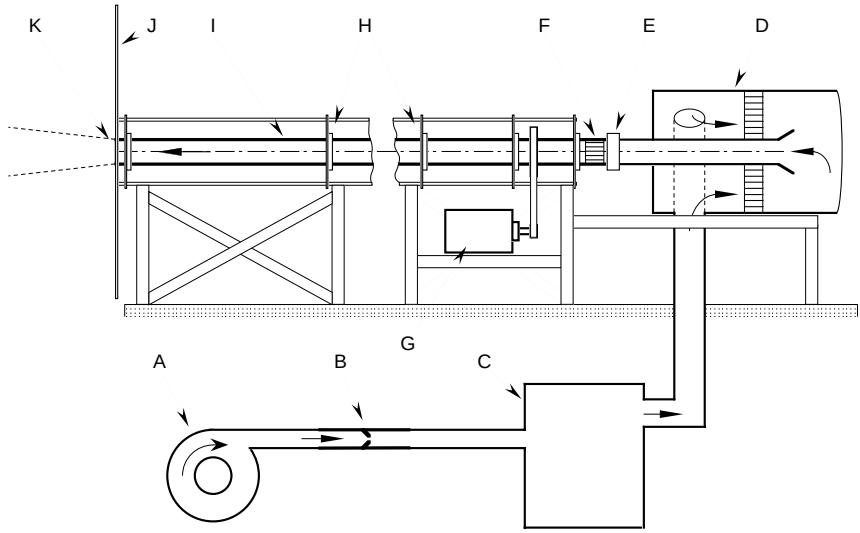

FIGURE 4.1. Schematic of the experimental setup. A) Fan, B) Flow meter, C) Settling chamber, D) Stagnation chamber, E) Coupling-box between rotating and stationary pipe, F) Honeycomb fixed to the pipe, G) DC-motor, H) Ball bearings, I) Rotating pipe with a length of 6 m and inner diameter of 60 mm, J) Aluminum plate, K) Pipe outlet.

4.1. Experimental apparatus

Figure 4.1 shows a schematic of the apparatus. The air comes from a centrifugal fan with a throttle at the inlet to allow flow adjustment, passes a flow orifice meter and is conveyed into a settling chamber to reduce fluctuations from the upstream flow system. From the settling chamber three pipes run radially into a cylindrical stagnation chamber distributing the air evenly. The flow passes an annular honeycomb to reduce lateral velocity components and to further reduce remaining pressure fluctuations one end of the cylindric settling chamber is covered with an elastic membrane. Finally, the air leaves the chamber through an axially aligned stationary pipe at the centre of the chamber. To achieve a symmetric smooth inflow the pipe is provided with an inlet funnel. The length of this pipe is 1 m and it is directly connected by a sealed coupling box to which on the other side the 6 m long rotaing pipe is connected.

The rotating pipe is made of seamless steel, has a wall thickness of 5 mm and an inner diameter of 60 mm. The inner surface is honed and the surface roughness is less than 5 micron, according to manufacturer specifications. The

pipe is mounted inside a rigid triangular shaped framework with five ball bearings supports. The rotation is obtained via a belt driven by an electric DC motor with a feedback circuit. This ensures a constant rotation rate up to the maximum rotational speed of 1800 rpm. The drive is located close to the upstream end of the pipe. The structure has been statically and dynamically balanced and a test for vibrations has been performed for the rotation rates used during the experiments.

In order to bring the incoming air into rotation, a twelve centimeter long honeycomb is placed inside the rotating pipe immediately downstream of the inlet. The honeycomb consists of 5 mm diameter drinking straws. Of course it is also located inside the pipe in the cases when the rotation speed is zero.

The outlet of the pipe is at the centre of a stationary rectangular (80 cm $\times$ 100 cm) flat aluminium plate of 5 mm thickness. The pipe end is edged and mounted in such a way that it is flush with the plate surface. The rotating surface at the pipe outlet is limited to a ring of 0.5 mm in thickness.

The flow emerges horizontally into the ambient still air 1.1 m above the floor and far away from any other physical boundaries in the laboratory.

The test pipe was originally designed for moderate rotation rates, however when the experiments were underway it was also decided to go to higher swirl rates. A complication is that for high rotation rates the outcoming jet undergoes vortex breakdown and this also affects the flow near the exit of the pipe. In order to be able to perform measurements of the pipe flow itself also at higher rotation rates a glass section was added to the end of the steel pipe. For this case the large end plate was removed and the glass pipe was mounted to the steel pipe via an aluminum coupling. The glass section was 0.2 m long, with an inner diameter of 60.3 mm and a wall thickness of 2.2 mm. The glass pipe hence has a slightly larger diameter than the steel pipe which gives a step of approximately 0.15 mm at the connection. These measurements were however done only for a Reynolds number of 12000 which gives a step height of less than two viscous length units.

As mentioned above an orifice flow meter is used to adjust and monitor the pipe flow rate. The orifice is located after 1.0 m of a 1.65 m long, 40 mm diameter pipe and the orifice has a diameter of 28 mm. The pressure difference across the orifice is measured by a calibrated pressure transducer (MPX10DP). The flow meter curve as shown in figure 4.2 directly shows the transducer voltage as function of the bulk velocity in the pipe and shows the expected near parabolic shape. The bulk velocity has been calculated via integration of the mean velocity profile at the pipe exit using data obtained from single hot-wire probe measurements in the non-swirling flow. The accuracy of such a calculation is hampered by the weightining by the radius, which makes it quite sensitive to measurement errors close to the pipe wall. However, this is of no major concern here since the main purpose of the flow meter is to monitor and ensure constant flow rates from day to day and to adjust the fan throttle to obtain a constant flow rate when varying the swirl rate.

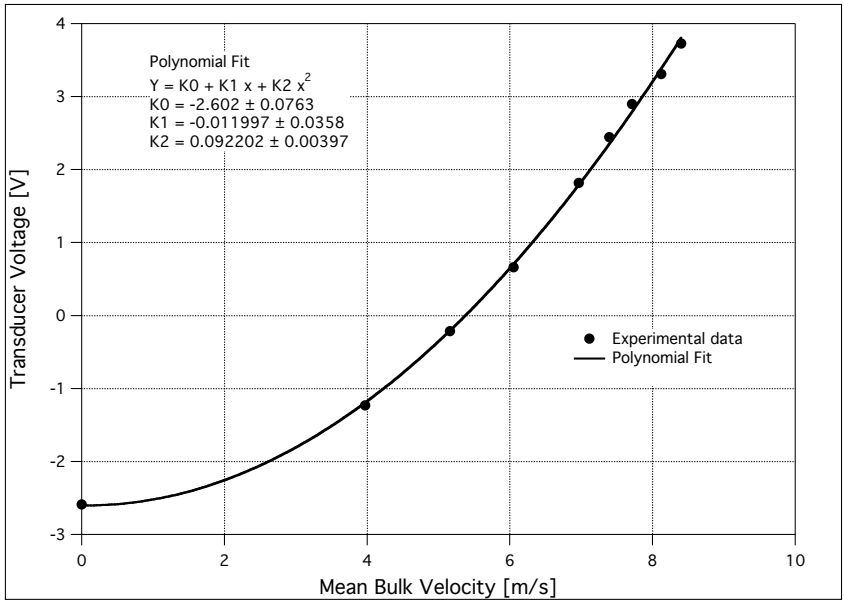

FIGURE 4.2. Pressure transducer calibration curve: the mean bulk velocity at the pipe exit is plotted versus the voltage from the pressure transducer. The pressure transducer has a linear response between pressure and voltage

A fully developed pipe flow in the non-rotating regime for the present Reynolds number range should be obtained for an L/D-ratio larger than typically 60. In the present study we investigated this in an indirect way by partially obstructing the honeycomb inserted at the inlet end of the rotating pipe with some plugs. No reminiscences of the plugs could be noticed in the flow which indicates that the flow has reached a fully developed turbulent state.

4.2. Measurement techniques

The velocity in the pipe and the jet was measured both with Laser Doppler Velocimetry (LDV) and hot-wire anemometry. The LDV system was a one component system, whereas for the hot-wire anemometry both single and X-wires were used. The advantage with the hot wire is both that two components (the streamwise and either the azimuthal or the radial components, depending on the X-wire orientation) could be measured simultaneously as well as that continuous time signals are obtained. The main problems are the large velocity gradients near the pipe wall and the large flow angles (and even backflow) in the outer part of the jet which can reach values where the hot-wire calibration is invalid. The LDV measurements on the other hand can handle these situations, however the one-component system could not generate simultaneous signals of the two velocity components.

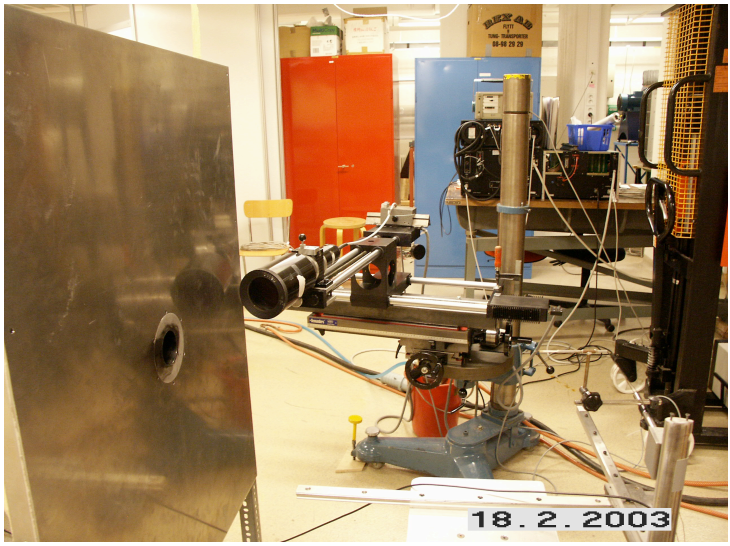

FIGURE 4.3. The LDV system in the inclined 12° configuration to measured at the jet exit.

4.2.1. *Laser Doppler Velocimetry*

Laser Doppler Velocimetry (LDV) has been used to obtain mean and fluctuating velocity components in all three (streamwise, azimuthal and radial) directions. For the present experiment LDV has certain advantages as compared to hot-wire anemometry. For instance in the rotating flow the flow angles with respect to the streamwise direction can be fairly large which may make the use of hot wires unaccurate or even impossible and in the outer parts of the jet even backflow may occur. Rotating flows may also be sensitive to disturbances and therefore a nonintrusive measurement technique is preferable.

The LDV system is a single component FlowLite system from DANTEC comprising a single velocity component backscatter fiber optics probe with a beam expander, a 310 mm lens and a signal analyzer of correlation type. The source is a He-Ne laser of 10 mW emitting light with a wave length of 632.8 nm. The system is equipped with a Bragg cell providing a 40 MHz frequency shift to be able to determine the flow direction. The LDV is calibrated by means of a rotating wheel with a well known angular velocity. The probe head is mounted on a 2D traversing system driven by a DC-motor with encoder in each direction. The optics can be rotated 90° along its optical axis to measure the second velocity component. The measuring volume, an elipsoide, has the dimensions: $0.81\times0.09\times0.09$ mm^3 with its main axis along the optical axis. Most of the measurements were carried out with the optical axis perpendicular to the pipe axis. Therefore, axial and azimuthal velocities could be measured directly.

However, in the close vicinity of the pipe orifice, due to the presence of the large aluminum plate, the inclination angle was changed 12° in order to

measure both velocity components at the outlet. The data at the pipe outlet do not cover the whole pipe diameter because, due to the inclination of the LDV system, scattered light saturated the photo detector when the laser beams approach the inner wall surface of the steel pipe. Figure 4.3 shows the set-up for LDV-measurements with the laser head on the traversing system. It also shows the pipe exit in the large rectangular end plate.

The data rate varied depending on the measurement position with the highest rate in the central region. The sampling was stopped either at 12000 samples or after 240 s. To acquire statistically independent samples the sampling rate was limited to 100 Hz.

The particles used for the LDV measurements are small droplets of condensed smoke of polyethylenglycol. They are injected into the air at the inlet of the centrifugal fan. No stratification of the particles in the outlet jet has been found, not even at the highest swirl rates.

4.2.2. *Hot-Wire Anemometry*

Hot-wire measurements were mainly made with X-wire probes. These measurements complement the LDV measurements, in that it provide two velocity components simultaneously and time signals for spectral analysis. The X-wire probes are made in house. The wire diameter is 2.5 μm and it is 1.3 mm long and the distance between the wires is 1.5 mm giving a measurement volume of about 1.1 mm in side length. The probes are calibrated in the potential core of a small laminar top hat velocity profile air jet (the same device has been used by Alfredsson & Johansson (1982), but with water) in a separate facility (figure 4.4) operating with air at the same temperature. Figure 4.5 shows a photograph of the calibration set-up with the hot-wire probe mounted on the device with which the angle of attack can be changed manually during the calibration.

The calibration procedure was similar to the one used by Österlund (1999) for which calibration points are obtained for a given set of velocities (typically 15 velocities) and probe inclinations (typical in intervals of 10 degrees, with larger angles at low velocities, up to $\pm$ 40 degrees). The calibration function is based on a 5th order polynomial approximation by least-squares fit of mean velocity and angle of attack of the probe (figure 4.6). For each point during the calibration the sampling rate has been fixed at 4000 Hz and the measurement performed for 30 seconds. The spectral analysis measurements in the swirling and non-swirling jet used a sampling rate of 10000 Hz and had a duration of 130 seconds. The velocity profile measurements used a sampling rate of 4000 Hz and a duration of 40 seconds close to the pipe exit ($x/D \leqslant 2$) and a duration of 60 seconds further downstream.

The velocity data obtained by the hot-wire technique are similar to the LDV data (and also to the Pitot probe and the single-wire data used as test in the non swirling case). Due to the presence of a considerable velocity gradients at some postions the X-wire data need an "a posteriori" correction procedure

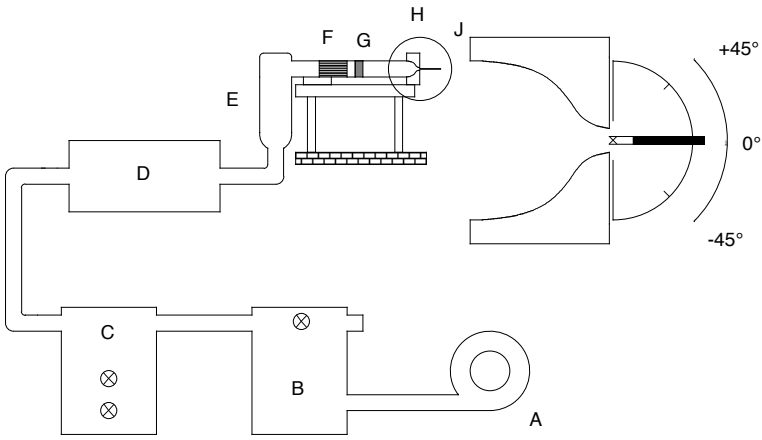

FIGURE 4.4. Schematic of the calibration jet setup. A) Fan, B) Settling chamber with seven valves, C) Settling chamber with two valves, D) Large stagnation chamber, E) Small stagnation chamber, F) Honeycomb, G) Sponge, H) Contraction, J) Holder for the X-wire to enable angular calibration.

similar to the one developed by Talamelli *et al.* (2000) and used to correct hot-wire measurements in the near wall region of a boundary layer. To measure simultaneously the axial and the azimuthal velocity components the X-wire probe is positioned with the two wires perpendicular to the traversed diameter. This configuration, due to the distance between the planes of the hot-wires, is particular sensitive to the strong velocity gradient of the investigated flow. The correction procedure make it possible to find out the mean velocity component from the measured ones ($\overline{U_m}$ and $\overline{V_m}$) in an iterative way according to equations 4.1 and 4.2. Δ represents the distance between the centres of the two wire but in this term it is possible to include all the geometrical uncertainties of the probe position.

$$\overline{U_m} = \overline{U} + \frac{\Delta}{2}\frac{\partial \overline{V}}{\partial y} + \frac{1}{2}\left(\frac{\Delta}{2}\right)^2 \frac{\partial^2 \overline{U}}{\partial y^2} + \cdots \tag{4.1}$$

$$\overline{V_m} = \overline{V} + \frac{\Delta}{2}\frac{\partial \overline{U}}{\partial y} + \frac{1}{2}\left(\frac{\Delta}{2}\right)^2 \frac{\partial^2 \overline{V}}{\partial y^2} + \cdots \tag{4.2}$$

Starting from a measurement with single hot-wire in a non swirling flow is possible to calculate $\frac{\partial \overline{U}}{\partial y}$ and, in the same flow $\overline{V_m}$ is measured with the X-wire. Then, since in such a flow there is no azimuthal velocity component (V=0),

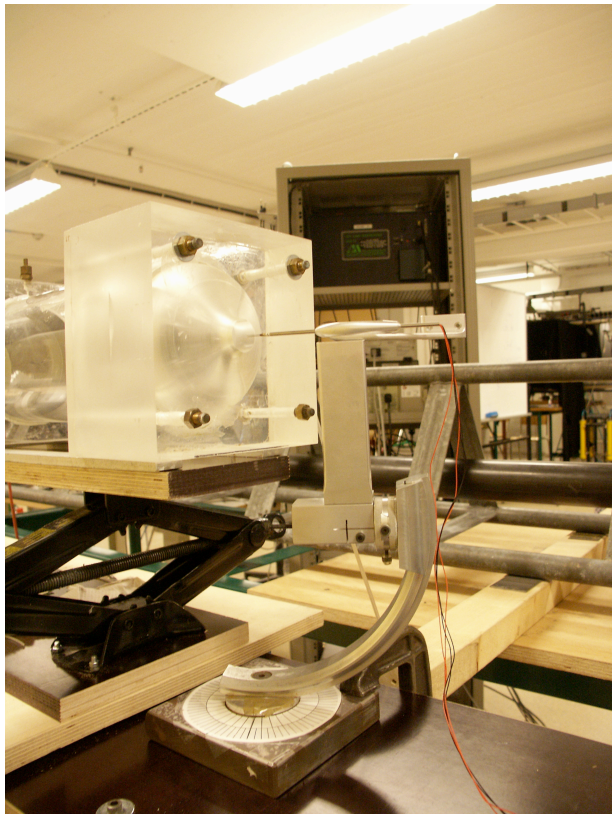

FIGURE 4.5. Calibration jet device: the hot-wire is positioned in the potential core of the laminar jet. The angle of attack is regulated manually and the velocity of the jet air by a system of valves.

neglecting in a first approximation the second order terms in 4.2, it is possible to estimate Δ that shows an almost constant value along the diameter of the pipe. Knowing Δ the correction is applied and the axial U and the azimuthal V velocity component are calculated including also the second order terms as shown in the equations.

4.2.3. *Flow visualization*

A few flow visualization photographs were taken of the jet development. The smoke used for the visualization is the same as applied for LDV measurements (polyethylenglycol). The flow was illuminated with a laser sheet from a 2 W Argon-Ion laser source and the photographs were taken by a digital camera (Minolta DiMage 7i).

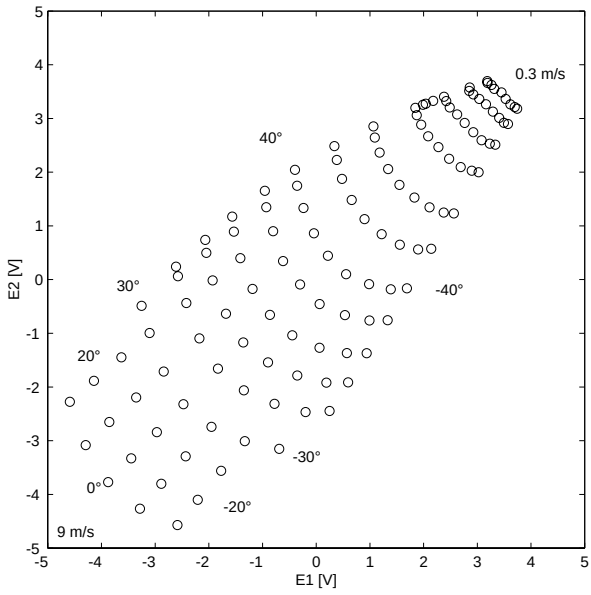

FIGURE 4.6. Example of calibration plot for the X-wire probe. The voltages from the two hot-wires identify the angle of attack of the probe and the velocity.

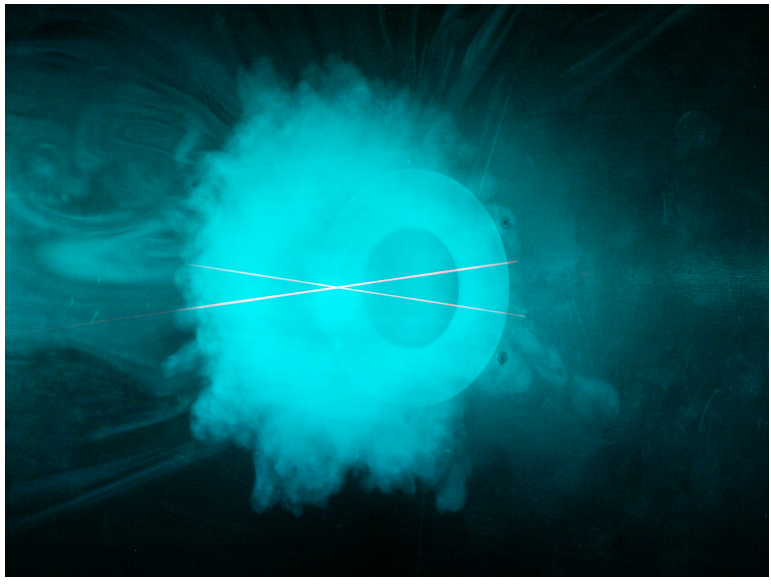

FIGURE 4.7. Flow visualization: the laser sheet cuts the swirling jet normally to the pipe axis at one diameter from the exit, seen as the dark hole in the centre. The two light beams are the LDV lasers that identify the centre of the jet one diameter downstream.

CHAPTER 5

Results for rotating pipe flow

The measurements in the rotating pipe have two aims, firstly it is done in order to complement and extend previous measurements of rotating pipe flow and to evaluate some new scaling ideas, secondly it is done in order to give accurate exit conditions for the jet flow.

The experiments were carried out at three Reynolds number, Re= 12000, 24000, 33500 for the swirl numbers, S= 0, 0.2, 0.5, 1.0, 1.5 (the two highest S values were only measured for Re=12000). Measurements were made both with X-probes and LDV. For the two highest swirl numbers the measurements were made inside the glass extension of the pipe, for all other measurements both the hot-wire and the LDV measurement volume were located at the pipe exit. However in the following mainly the LDV-data will be shown, although most measurements were also taken with the X-wire. In general one may say that the agreement between the two metods is good, however the hot-wire measurements were slightly affected by temperature drift and therefore not as accurate in absolute terms.

In the figures a radial traverse of the measurement position corresponds to a horizontal traverse in the laboratory frame of reference. Although the radius r be definition always is positive we give values of r on the left-hand side of the jet (looking from upstream) negative values.

5.1. The flow field

5.1.1. *Mean flow data*

We first start with showing the mean streamwise velocity profiles for all three Reynolds numbers at S=0 and 0.5 in figure 5.1. All data have been normalized with the bulk velocity, which is taken from the flow meter measurements. No data could be obtained close to the wall at the right hand side (r/R >0.9) of the set up since reflections of the laser light in the pipe wall disturbed the measurements. As can be seen there is not a very large difference between the Reynolds numbers, the non-rotating cases fall on top of each other and in principle also the ones for S=0.5, however they show a slight systematic variation. The most obvious result in the figure is however that the rotation cases show a much more peaked velocity profile, i.e. the centreline velocity is higher, showing the tendency previously observed that the profile tends towards a parabolic shape. In fact one would expect a slightly larger effect of the swirl

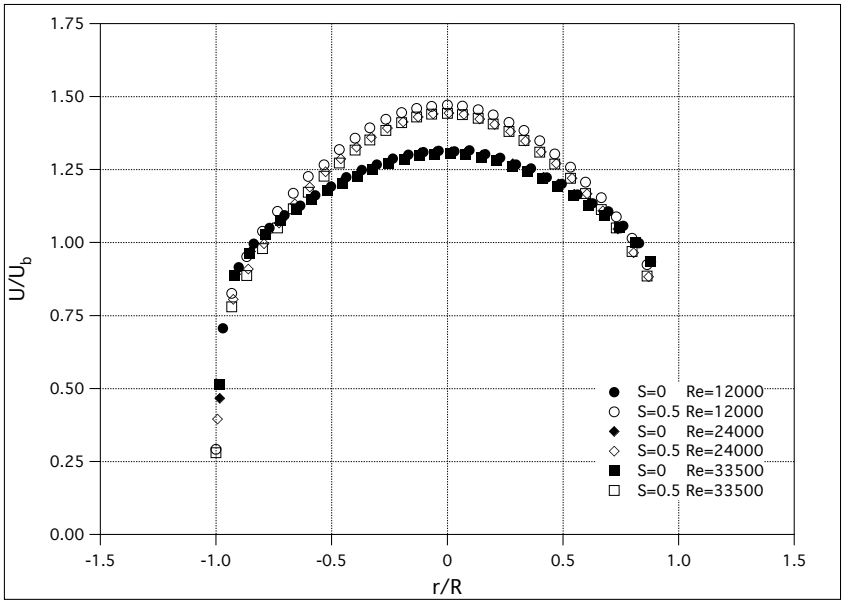

FIGURE 5.1. Streamwise mean velocity measured at the pipe outlet for three Reynolds numbers (Re =12000, 24000, 35000) and two swirl numbers S=0, 0.5.

for low Reynolds numbers, which is the trend observed here. The increase of the velocity at the centreline with rotation gives a corresponding decrease of the velocity close to the wall. This causes a decrease of the wall friction hence decreasing the overall pressure losses of the set-up. During the experiments the upstream valves were adjusted to keep the flow rate and hence Reynolds number constant when the swirl was increased.

In figure 5.2 the mean azimuthal velocity is shown across a full diameter of the pipe for S=0.5. As can be seen all three Reynolds numbers show a similar distribution and seem to follow the parabolic curve (solid line) very close. At a first sight, it may be surprising that the mean flow field of a rotating pipe flow deviates from solid body rotation, but as previously described the difference as compared to the non-rotating case is that the Reynolds stress $\overline{vw} \neq 0$, which through eq. (1.12) make the azimuthal profile deviate from the linear one. In fact we can use eq. (1.12) to determine the distribution of $\overline{vw}$ if the mean profile of V is known and by assuming a parabolic velocity distribution

$$\frac{V(r)}{V(R)} = \left(\frac{r}{R}\right)^2$$

it is possible to integrate eq. (1.12) analytically to obtain

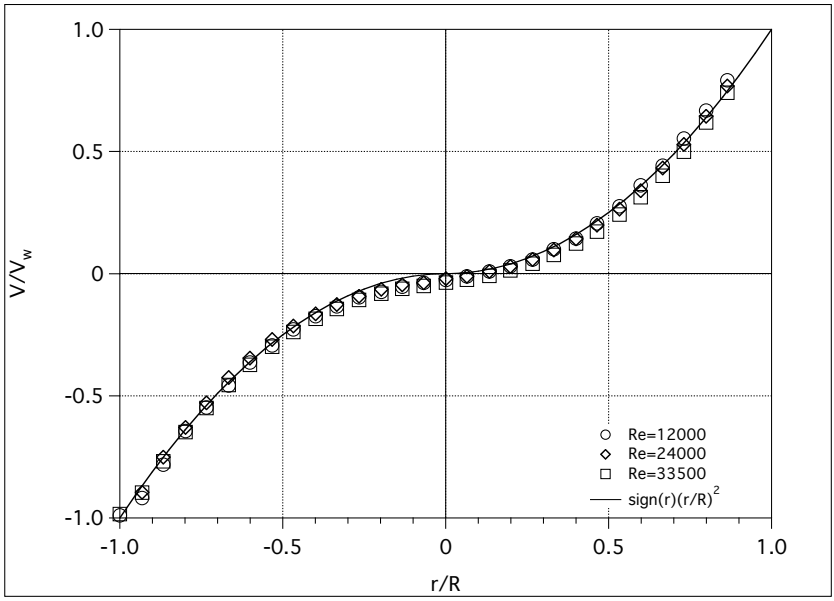

FIGURE 5.2. Mean azimuthal velocity. x/D=0, S=0.5 .

$$\frac{\overline{vw}}{U_b^2} = \frac{2S}{Re}\frac{r}{R} \tag{5.1}$$

Equation (5.1) shows that the distribution of $\overline{vw}$ varies linearly with r. However, this expression is of course not valid near the wall, since at the wall itself ($r = R$) both v and w have to be zero, and hence $\overline{vw}$ =0. That a parabolic profile in V would lead to a linear distribution of $\overline{vw}$ was first pointed out by Facciolo *et al.* (2003). The numerical simulations by Orlandi & Fatica (1997) also show a rather linear profile and their data are plotted in figure 5.3 together with the linear relationship. As can be seen the overall agreement is good. Also the data of Speziale *et al.* (2000) shows a near linear relation between $\overline{vw}$ and r.

In the other part of this study swirling jets are investigated and for that case it is interesting to define a swirl number based on the velocity profiles according to eq. 1.23. From the measured velocity profiles at the pipe outlet it has been possible to make accurate calculations of this value which are shown in table 5.1. The table shows only small change in the values of the swirl number for all the Reynolds number investigated, which indeed is a measure on the similarity of the profiles. It can also be seen that the integrated swirl number has a numerical value of about one third compared to the value used for the pipe flow.

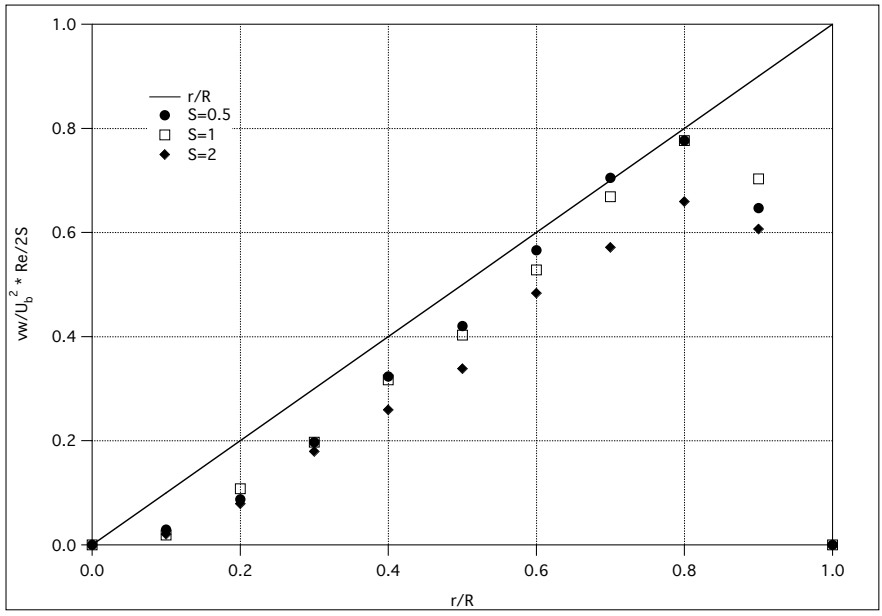

FIGURE 5.3. The theoretical distribution of $\overline{vw}$ (eq. 5.1) compared with DNS data from Orlandi & Fatica (1997). The Reynolds number used in the simulation is $Re = 4900$.

S	V_w/U_b	$G_\theta/(G_x R)$
Re=12000	0.2	0.064
	0.5	0.151
Re=24000	0.2	0.064
	0.5	0.152
Re=33500	0.2	0.064
	0.5	0.156

TABLE 5.1. The swirl number calculated at the pipe exit.

5.1.2. *Turbulence distributions*

In this section we present some measurements of turbulence data taken mainly with the LDV equipment. First we present a comparison between u_{rms}-profiles (u'/U_b) in the non-rotating and rotating cases (S=0 and 0.5). The data show a clear trend that the rotating cases have lower values as compared to the non-rotating ones at the same Reynolds number, although the difference is not large. The difference is most evident at the centreline. With the present scaling the data are presented in "absolute" terms and if the data instead had been normalized with the centreline velocity the differences had become larger.

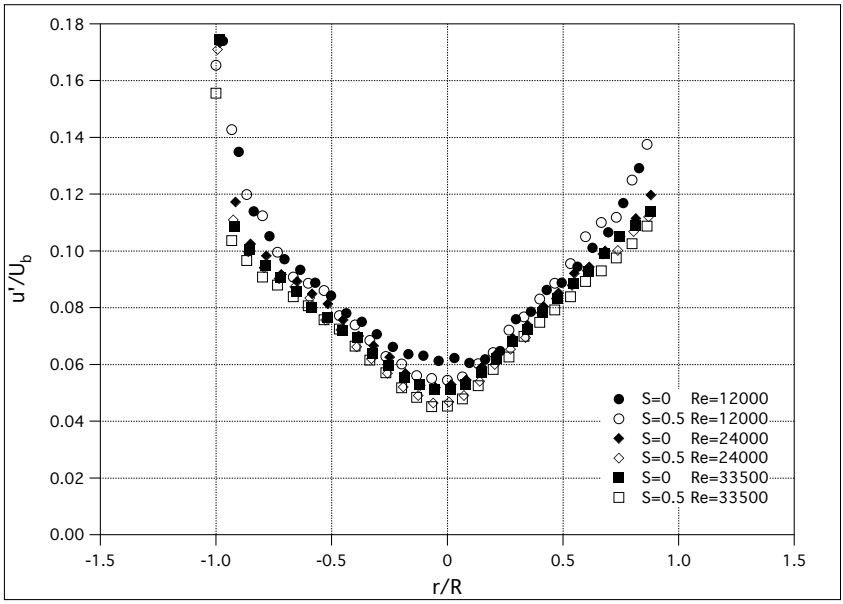

FIGURE 5.4. Streamwise turbulence intensity at x/D=0, S=0, 0.5 for the three Reynolds numbers. Same data as in figure 5.1

In figure 5.5 the v_{rms}–profiles (v'/U_b) are plotted. Unfortunately there are no available data for S=0, however the two swirl numbers seem to overlap nicely in the central part of the pipe whereas closer to the wall the level is lower for the high swirl number. The present trends both for u_{rms} and v_{rms} are in accordance with the measurements by Imao *et al.* (1996) who also observed a decrease with increasing rotation, however in the numerical simulations by Orlandi (1997) and Satake & Kunugi (2002) the trend is the opposite.

We also show a plot with the data of all three velocity components in order to demonstrate their relative magnitudes in the pipe in figure 5.6. For the present swirl rates this figure is qualitatively similar to what one would expect for the non-rotating case.[1]

[1]It should be noted that the measurements of w_{rms} at x/D=0 is the result of an indirect measurement aimed at determining the Reynolds stress component $\overline{vw}$. This was done by tilting the laser head at ±45 degrees and making two measurements. By adding or subtracting the square of the two signals either $\overline{vw}$ or $(\overline{v^2} + \overline{w^2})$ are obtained. In order to obtain $\overline{w^2}$ the separate measurements of $\overline{v^2}$ were subtracted. Only measurements on one side of the jet were done, so these data have been mirror imaged in the figure. Due to the subtraction of two large numbers the accuary of the measurements of $\overline{vw}$ were unfortunately found to be to low to give useful results.

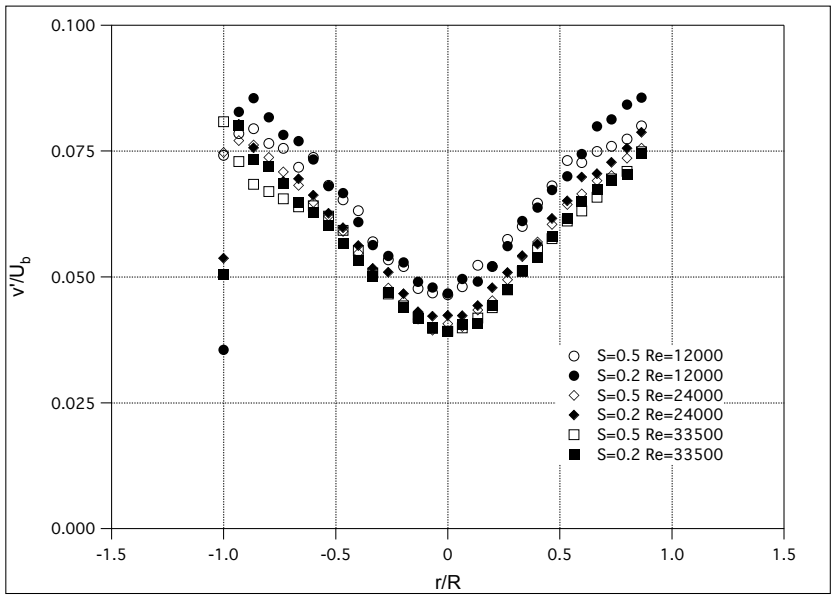

FIGURE 5.5. Azimuthal turbulence intensity at x/D=0, S=0.2, 0.5 for the three Reynolds numbers. The S=0.5 results are evaluated from the same data as in figure 5.2

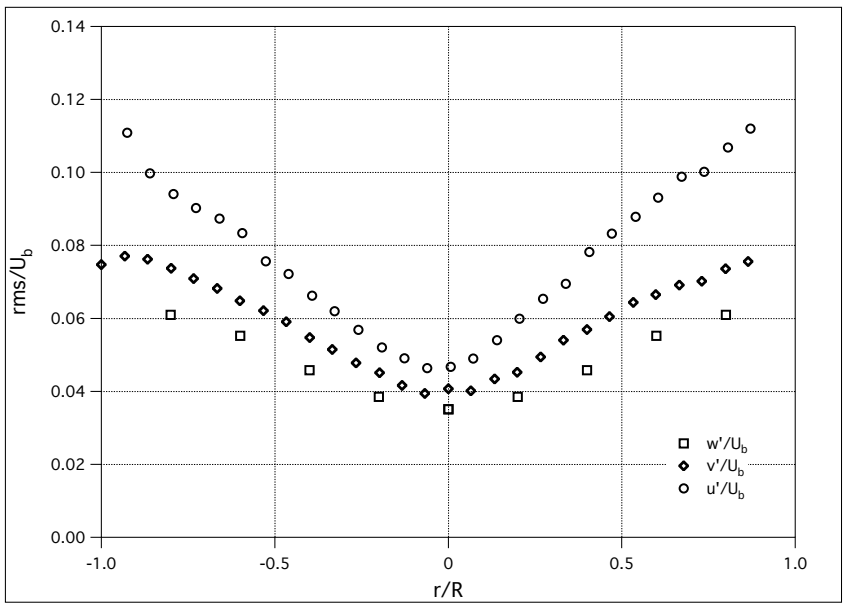

FIGURE 5.6. Comparison between the axial, azimuthal and radial turbulence intensity at the pipe outlet for S=0.5 Re=24000.

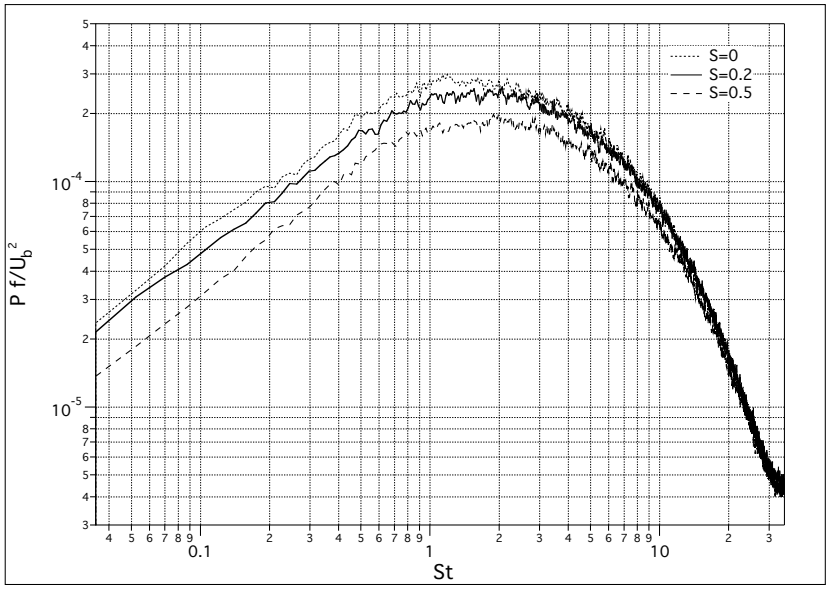

FIGURE 5.7. Spectra of u' at the outlet centreline measured with the X-probe. Re=33500.

Finally we show typical spectra of the streamwise velocity measured at the jet exit (figure 5.7) on the centreline. The spectra are plotted as the frequency times the spectral density ($f \cdot P$) which directly show the region of maximum energy content. They are also normalized by the bulk velocity so a comparison between them directly give for which frequencies the turbulence has been affected. The frequency axis is normalized to show the Strouhal number ($St = fD/U_b$). As can be seen the energy density decreases with increasing rotation which is consistent with the data in figure 5.4. For the present data there is about a 10 % decrease in the values of u_{rms}/U_b when the swirl numbers increase from S =0 to 0.2 and a further decrease of 10 % when S =0.5.

5.2. Scaling of the mean flow field

In the following we will describe the streamwise mean velocity field in some different scalings. Typically a turbulent velocity profile is described in terms of the viscous sublayer, a buffer region, a logarithmic region and then finally a wake region. The logarithmic region is usually written as

$$\frac{U}{u_\tau} = \frac{1}{\kappa} \log \frac{y u_\tau}{\nu} + B \tag{5.2}$$

where u_τ is the friction velocity and $y = R - r$. The present measurements do not allow us to determine the friction velocity by extrapolating the mean velocity profiles to the wall and we will instead use the centreline velocity (U_c) as the velocity scale. In figure 5.8 the streamwise mean velocity data have been plotted in a semilogarithmic diagram. As can be seen in the figure the non-rotating case shows a typical logarithmic region up to $y/R \approx 0.3$. The full drawn line corresponds to

$$\frac{U}{U_c} = \frac{1}{K} \log \frac{y}{R} + C \tag{5.3}$$

with K=8.2 and C=0.97. The relation between the Karman constant κ and the constant Kin eq. 5.3 can be written

$$K = \frac{U_c}{u_\tau} \kappa \tag{5.4}$$

and the additive constant

$$C = \frac{u_\tau}{U_c} \left(\frac{1}{\kappa} \log \frac{R u_\tau}{\nu} + B \right) \tag{5.5}$$

If one wants to convert the data for the S=0 case to standard values one has to find the ratio of U_c/u_τ from friction factor data. At Re=12000 a good approximation of this ratio is 20.5 which would give us corresponding values of κ= 0.40 and B=4.0. Also the mean velocity distributions for low swirl numbers (S=0.2 and 0.5) seem to exhibit a logarithmic region albeit with a different slope as compared to the non-rotating case. It is also clear that the extent of the logarithmic region becomes smaller when S increases. For the high rotation rates (S=1.0 and 1.5) only two points on each set of measurements lie on a line with that slope so it is not possible to draw any conclusions, but future experiments and simulations may want to study if this scaling is valid also for higher S.

Table 5.8 also include data points taken from the simulation of Satake & Kunugi (2002) (S&K in the table). The data are derived from their figure 3 with a logarithmic line fitted by eye. However these data seem to consistently show a lower value of K. This may be a Reynolds number effect since their Re was only 5300.

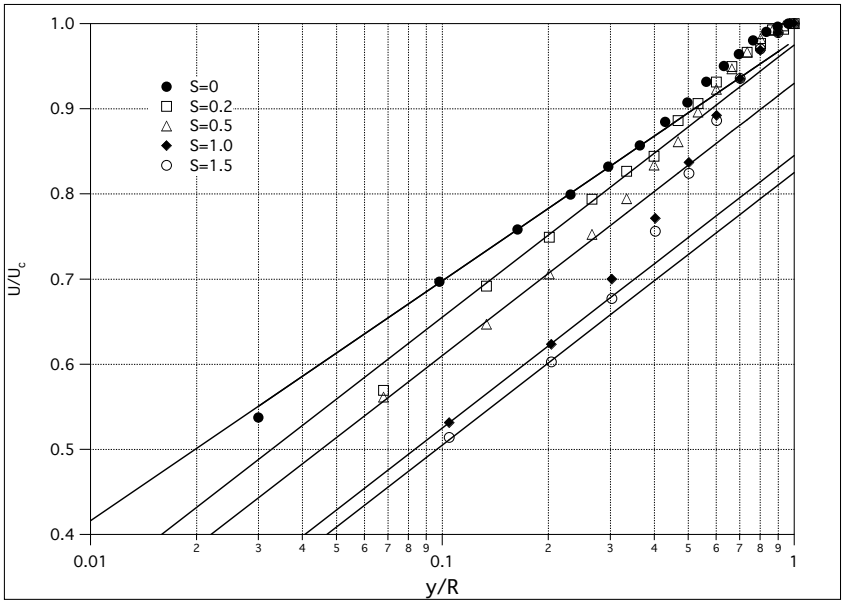

FIGURE 5.8. Streamwise mean velocity data at $Re = 12000$ for various values of S. The straight line for S =0 corresponds to K=8.2 whereas all other lines have K=7.2.

	$S\&K$			Present
S	κ	u_c/u_τ	K	K
0	0.40	19.5	7.8	8.2
0.5	0.22	22.3	4.9	7.2
1.0	0.22	24.0	5.2	*(7.2)*
1.5	No Data			*(7.2)*
2.0	0.18	26.7	4.9	No Data

TABLE 5.2. Determination of the slope of the logarithmic region for the data in figure 5.8 as well as for the data of Satake & Kunugi (2002).

5.2.1. *Scalings due to Oberlack (1999)*

In the analysis by Oberlack (1999) on stationary and rotating turbulent pipe flows, several scaling laws were suggested. In the following we will show some comparisons of our data at the lowest Re=12000 with the suggested scalings. The data used are first plotted in standard form in figure 5.9.

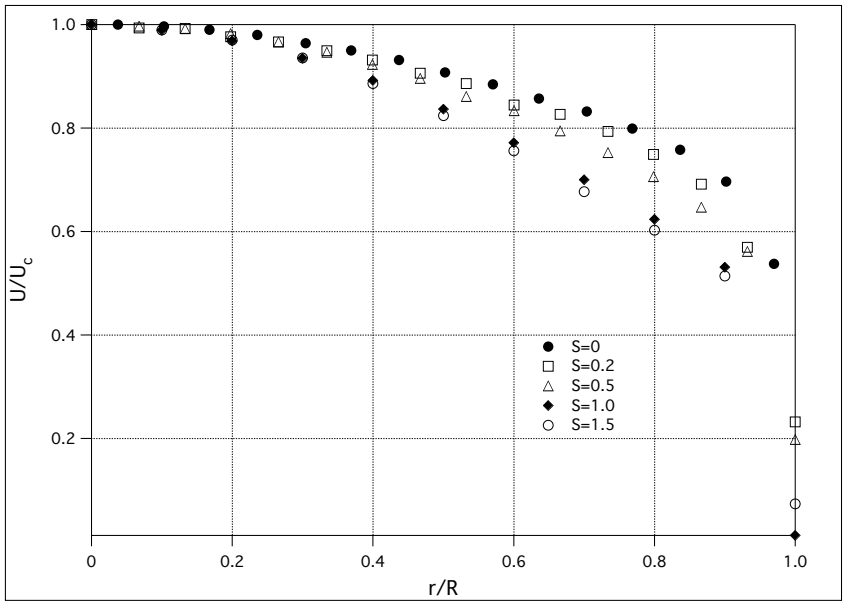

FIGURE 5.9. Mean streamwise velocity data for Re=24000 at five values of S.

One of the scaling laws suggested by Oberlack (1999) is that the mean streamwise velocity profile should have a logarithmic behaviour in the outer part of the flow. In his paper he plotted the data of Orlandi & Fatica (1997) and found such a behaviour in the region $0.5 < r/R < 0.8$. In figure 5.10 the present data are plotted in the same way, however a logarithmic region is not as evident as in the data of Orlandi & Fatica (1997). In this figure we have three different values of S and we have fitted lines both with the slope suggested by Oberlack (1999) which gives different regions of fit for the different S. We have also fitted a line in the same region as suggested by Oberlack ($0.5 < r/R < 0.8$) but then the lines will have different slopes, for S=0.5, 1.0 and 1.5 the values are λ= – 2.6, – 1.5 and – 1.1, respectively.

Figure 5.11 shows the mean velocity data plotted as the velocity defect $(U_c - U)$ normalised with the wall velocity (V_w) as function of r/R. In the figure we have also plotted lines with a slope assuming a quadratic relationship between the velocity defect and the radius. According to the theory of Oberlack, the exponent should be the same as for the azimuthal velocity (see eqs. 2.1 and 2.2) and since we have observed a parabolic velocity distribution for the azimuthal velocity (see figure 5.2) this exponent should then be equal to 2. As can be seen the measurement data show the expected linear (in the log-log-plot) behaviour over a large part of the channel. As can also be seen the data are displaced downwards with increasing S. This is to be expected

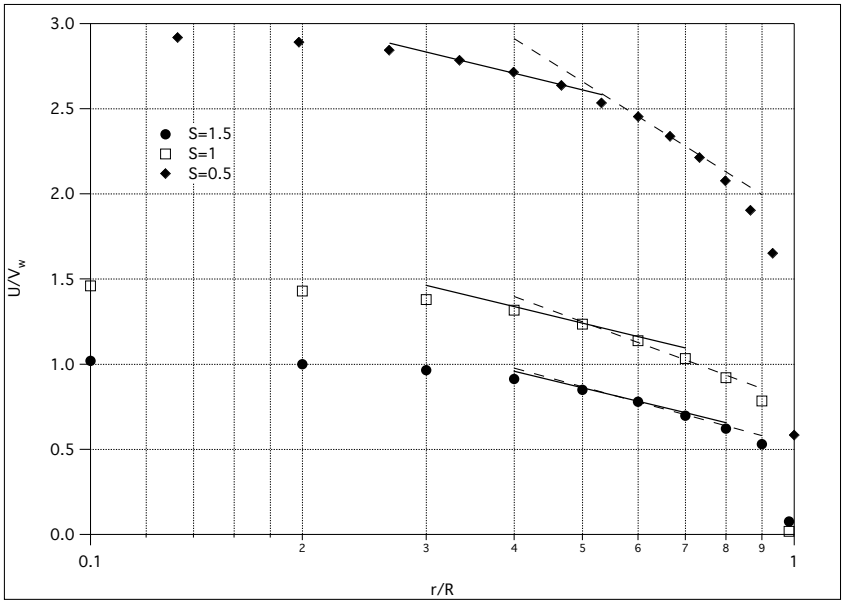

FIGURE 5.10. Mean streamwise velocity U normalised with the wall velocity (V_w) as function of r/R for three different swirl numbers at Re=12000.

since at the wall itself U=0 and there the value would hence be U_c/V_w which can be written $U_c/(U_bS)$, i.e. it is inversely proportional to S. There is of course also a slight variation (increase) of U_c/U_b with S which will tend in the other direction.[2] The slope of the lines corresponds to a quadratic behaviour and as can be seen the data seem to follow this slope closely. All in all figure 5.11 seems to be in accordance with the scaling suggested by Oberlack (1999).

[2]The ratio U_c/U_b for the three swirl numbers in figure 5.11 are 1.47, 1.48 and 1.55 for S=0.5, 1.0 and 1.5, respectively.

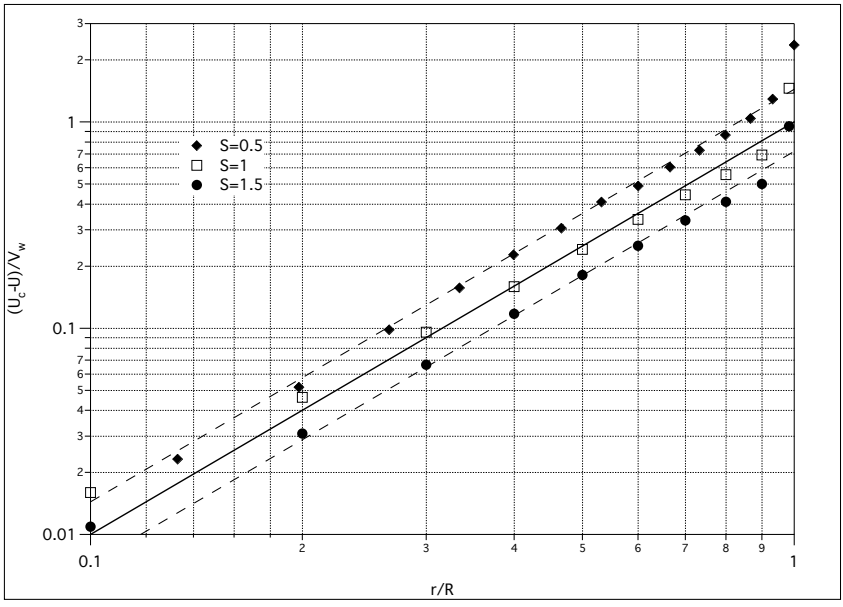

FIGURE 5.11. The velocity defect $(U_c - U)$ normalised with the wall velocity (V_w) as function of r/R for three different swirl numbers at Re=12000.

CHAPTER 6

Results for swirling jet flow

This chapter deals with measurements in the near-exit region of the jet, up to $10D$ downstream of the jet exit plane. Section 6.1 deals with the mean flow development, whereas section 6.2 shows the behaviour of all three fluctuating velocity components. Finally section 6.3 discusses the instantaneous flow angles and the limitations of hot-wire versus LDV-measurements in the jet.

6.1. Mean flow development

The evolution of the mean axial velocity profile at three downstream positions with and without swirl is shown in figure 6.1. Here we have chosen to present the data for Re=24000 at S=0 and S=0.5, but similar measurements were also made for the other values of the flow parameters (Re and S). The graphs clearly show how the intial profile at the pipe outlet is more peaked for the swirling flow case. At short distances downstream of the pipe outlet, $x/D \leq 2$, the axial velocity in the central region of the jet is fairly unaffected, whereas further downstream at $x/D = 6$, i.e. downstream of the potential core region, the velocity in the central region becomes significantly smaller for the rotating case. It is interesting to note that the figure shows that the different profiles have a common crossing point at about $\mid r/R \mid = 1$ and U/U_b=0.6, a characteristic that is also found in the other measurements at Reynolds number Re=12000 and Re=33500 and at S=0.2.

Figure 6.2 shows the downstream evolution of the normalised mean azimuthal velocity (V/V_w) profiles. As shown in chapter 5, the velocity profile at the pipe outlet closely follows a profile proportional to $(r/R)^2$. The figure shows that further downstream the radius of the potential core decreases but the "parabolic" nature of the azimuthal velocity seems to persist in the central region as long as the jet is not fully developed. An interesting observation is that at x/D=6 it seems that the v-component changes sign in the central region. The values here are quite small and it is not yet clear if this is a true physical observation.

The radial component of the mean velocity field was only measured for one swirl number S=0.5 and at x/D=2 and 6 (since at x/D=0 it should be zero). The mean radial component normalised with the bulk velocity is shown in figure 6.3. It is seen to have a maximum around r/R=1 at both x-positions and at larger r it decreases. At x/D=6 the radial velocity is larger, especially in the central region, it reaches a maximum roughly at the same radial position

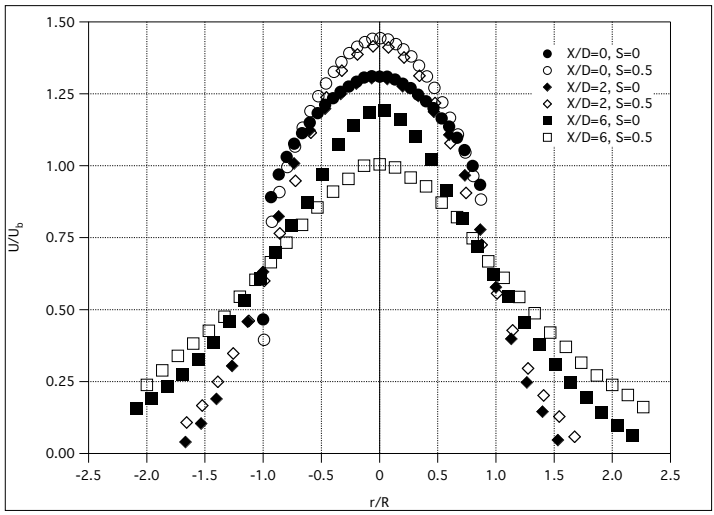

FIGURE 6.1. Mean axial velocity: Re=24000, S=0, 0.5.

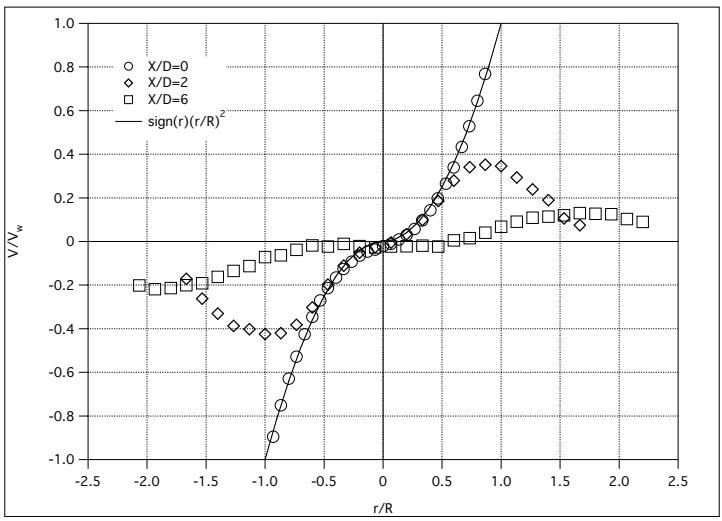

FIGURE 6.2. Mean azimuthal velocity. Re=24000, S=0.5.

as for x/D=2 and at the same level. In the outer region it then decreases more slowly. The behaviour of the radial component can be understood from the time-averaged continuity equation, which for the axisymmetric case becomes (see also eq. 1.1)

$$\frac{\partial W}{\partial r} + \frac{W}{r} + \frac{\partial U}{\partial x} = 0$$

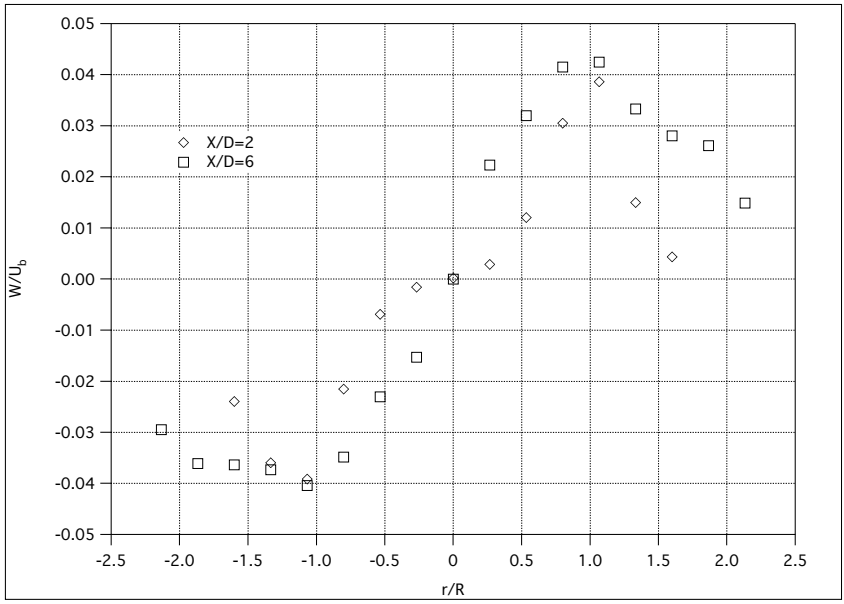

FIGURE 6.3. Mean radial component at Re=24000 S=0.5.

Since the streamwise mean velocity U increases with x in the outer part (for $r > R$) of the jet, $\frac{\partial U}{\partial x}$ is positive there and hence negative for $r < R$. W is directed outwards in this region and is therefore positive. This means that $\frac{\partial W}{\partial r}$ needs to change sign, from positive to negative, when r increases, which is also observed in figure 6.3.

6.1.1. *Flow entrainment*

An interesting variable of the jet is the entrainment of outer fluid into the jet. The entrainment may be obtained by integrating the streamwise velocity across the $r\theta$-plane which then will give the total axial flow. We will denote this quantity by Q and normalise it with Q_0, which is the axial flow coming from the pipe. This ratio is denoted the entrainment coefficient. However, the calculation may be affected by a significant uncertainty. Indeed, the flow in the outer part of the jet is measured with difficulty due to the very low velocities and may give large error contributions due to the weighting with the radius. To reduce this problem a least square fitting procedure (using a Gaussian function to estimate the tails of the profiles) was used in order to extrapolate the mean velocity profiles in the external part of the jet. The flow rate values are reported in Table 6.1. The accuracy of the above measurement was assessed by checking that the overall amount of flow momentum remains constant moving downstream for S=0. These values are also given in the table

		Q/Q_0			G_x (N)
Re	x/D	S=0	S=0.2	S=0.5	S=0
12000	2	1.53	1.62	2.00	0.0373
	6	2.49	2.81	3.15	0.0404
24000	2	1.43	1.52	1.58	0.143
	6	2.36	2.47	2.92	0.145
33500	2	1.37	1.40	1.52	0.272
	6	2.20	2.33	2.72	0.260

TABLE 6.1. The entrainment coefficient (Q/Q_0) for three different swirl numbers. As a comparison the constancy of the axial momentum flux (G_x) for the S=0 case was also checked using the same data.

and as can be seen they show a reasonable constancy between the two positions, giving confidence in the calculation of the entrainment coefficient.

Table 6.1 shows that an increase of the flow rate is observed by moving downstream for all the configurations analysed. This is due to the engulfment of ambient fluid by the vortical structures and by turbulent mixing. The swirl increases significantly both the entrainment and the jet spreading. This is also confirmed by the flow visualisations shown in figure 6.4. This enhancement of the entrainment due to the pipe rotation seems to be reduced by increasing the Reynolds number. The reason for this Reynolds number dependence is not clear. By looking at the flow visualisations it may be concluded that it is an effect related to the more pronounced eddy structures formed in the mixing layer at low Re, which may enhance the entrainment of fluid from the environment.

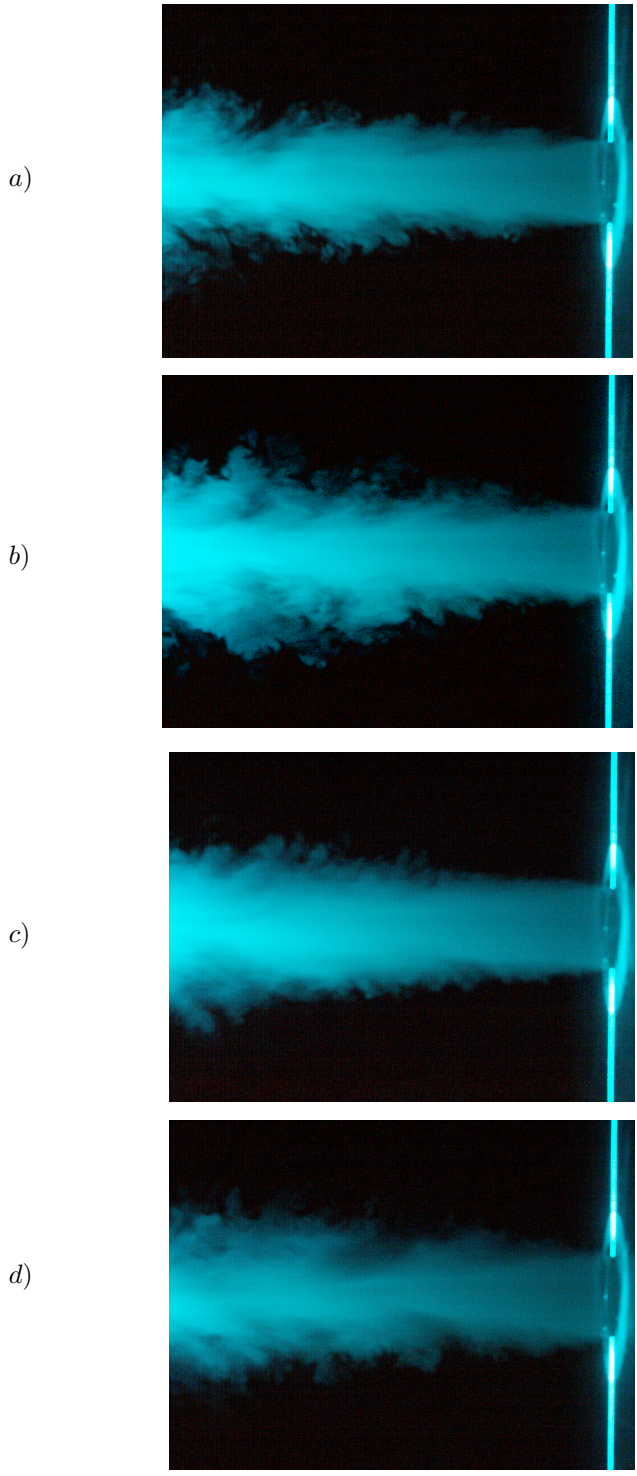

FIGURE 6.4. Smoke flow visualization. a) Re=12000, S=0, b) Re=12000, S=0.5, c) Re=24000, S=0, d) Re=24000, S=0.5

6.1.2. *The axial decay*

The mean axial velocity along the centreline, U/U_b, its dependence on swirl rate and Reynolds number are shown in figures 6.5 and 6.6. The figures display that the axial development of the jet from the pipe outlet to x/D=10 could be separated into two regions, i.e. the mixing region and the transition region (see Beér & Chigier (1972)). The first region extends from the pipe exit to 3–4 pipe diameters downstream, where the potential core ceases, while the second region covers the incipient part of the developing jet flow.

Close to the outlet the velocity decay along the axis is small, approximately linear and the axial velocity becomes higher with increasing swirl rate as has been observed at the pipe outlet (cf. figure 5.1). The small decrease of the axial velocity going downstream is explained by the flattening of the velocity profile in the central part of the core whereas the increase in centreline velocity is due to the development of a less blunt velocity profile at the outlet with increasing rotation (see figure 6.1).

In the region downstream of the potential core the velocity decrease is substantially larger than without rotation and increases with swirl rate whereas the variation in slope with Reynolds number is small. Another effect of the swirl seen in the figures is the influence on the form of the velocity decay curve. Without any swirl the decay is almost linear but for increasing swirl the straight line becomes gradually more curved.

Included in figure 6.6 are also data from the experiment by Rose (1962). That experiment is similar to the present in that the jet emerged from a stationary and rotating pipe with $L/D = 100$ at about the same Reynolds number. The data from the non-rotating cases fall on top of each others while in the rotating case the trend is the same but the fall off is still higher which may be partly explained by the somewhat higher swirl number (S=0.63).

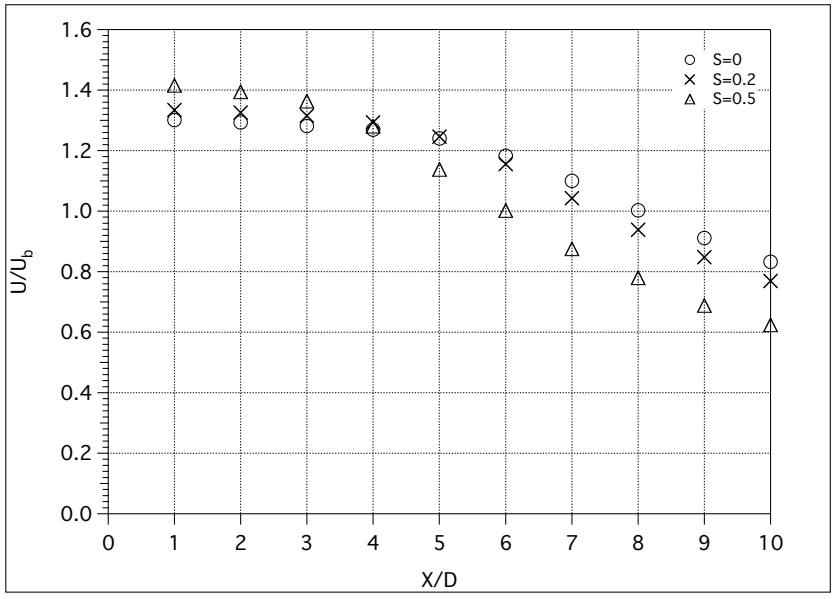

FIGURE 6.5. Axial velocity at the centreline Re=24000, S=0, 0.2, 0.5.

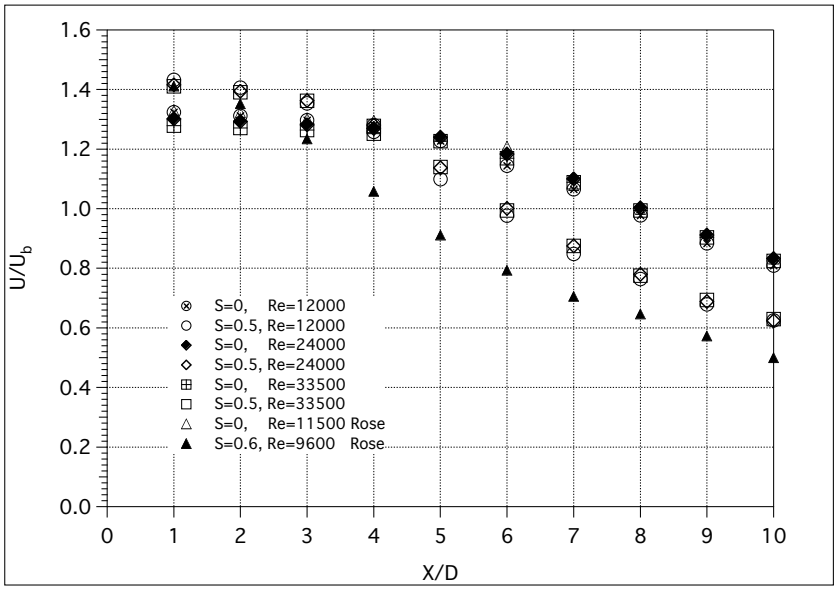

FIGURE 6.6. Axial velocity at the centreline. Re=12000, 24000, 33500; S=0, 0.5.

6.2. Turbulence development

This section deals with the development of the turbulence distributions across the jet. Profiles have been measured at the pipe outlet (x/D=0) and at two downstream positions (x/D=2 and 6). We chose to show data for Re=24000 and S=0 and 0.5 although profiles have been taken also for other flow parameters.

6.2.1. *Streamwise velocity fluctuations*

In figure 6.7 the streamwise turbulence intensity (u'/U_b), is compared for a jet with and without swirl at Re=24000 and three different downstream positions, x/D=0, 2 and 6. Only small differences close to the centreline are observed at the pipe outlet. Further downstream the turbulence intensity u'/U_b increases and at x/D=2 both profiles have a maximum around r/R=0.8. At x/D=6 the main difference between the swirling and non-swirling jet is found around the centreline where the turbulence level is almost doubled as the swirl number S goes from 0 to 0.5.

The higher moments of the axial velocity with and without swirl at Reynolds number 24000 are shown in the figure 6.8. Also here we have plotted the data for the S=0 and S=0.5 cases in the same diagram. Data points were taken across the full width of the jet, but since higher moments need more data these points had more scatter. Since the jet is axisymmetric we decided to take the average of the points measured at equal r-positions at both sides of the centreline and in that way the scatter was decreased. In the figures the data for each x/D are shifted in the vertical direction but the thicker horizonal lines in each figure shows the zero-level for the skewness and the Gaussian level of three for the flatness.

At the pipe outlet both skewness and flatness are only marginally influenced by the swirl rate which is clearly shown in the figures and in line with the u' results. The skewness rises from -0.5 at the centre to around 0 close to the wall while the flatness decreases from 3.5 to 2.8 in the corresponding points. These data could be compared with results obtained by Eggels *et al.* (1994) in non swirling pipe flow at $Re \approx$7000. Data are not provided over the whole pipe radius, but at r/R=0.5 skewness and flatness are -0.5 and 3.2 respectively and at r/R=0.9 they are 0 and 2.2 respectively which is close to our findings. The strong influences by rotation are found around the centreline, $\mid r/R \mid \leq$ 0.5, at x/D=6 and in the mixing layer at position x/D=2. At the central region downstream of the potential core (x/D=6) both skewness and flatness changes dramatically with the rotation rate whereas the influence is small at other radial positions. At the centreline, increasing the swirl number, the skewness increases and the flatness decreases from -1.2 to -0.3 and from 4.8 to 2.5 respectively.

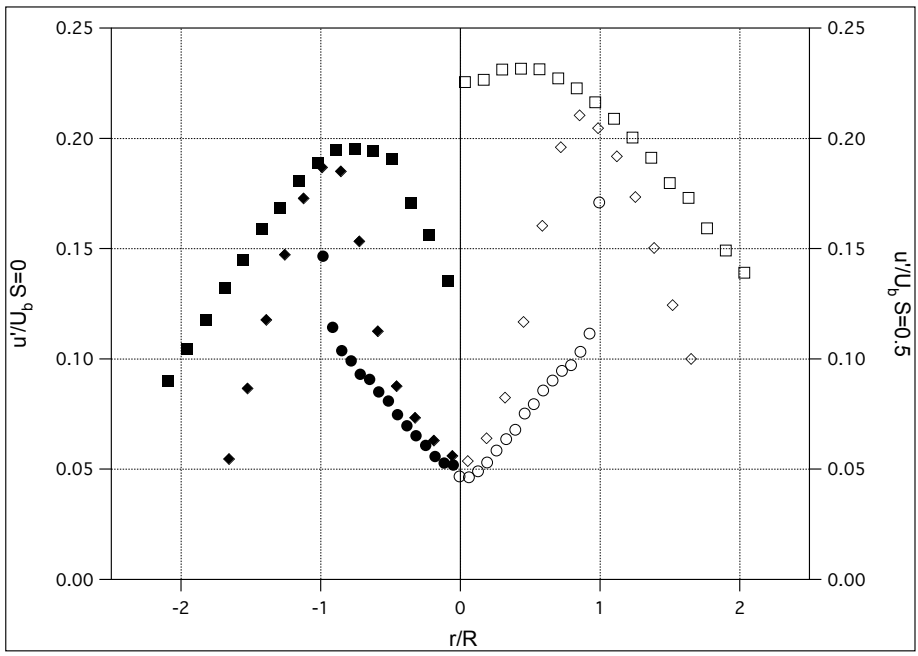

FIGURE 6.7. Axial turbulence intensity at Re=24000, S=0 and S=0.5, see fig 6.1 for symbols.

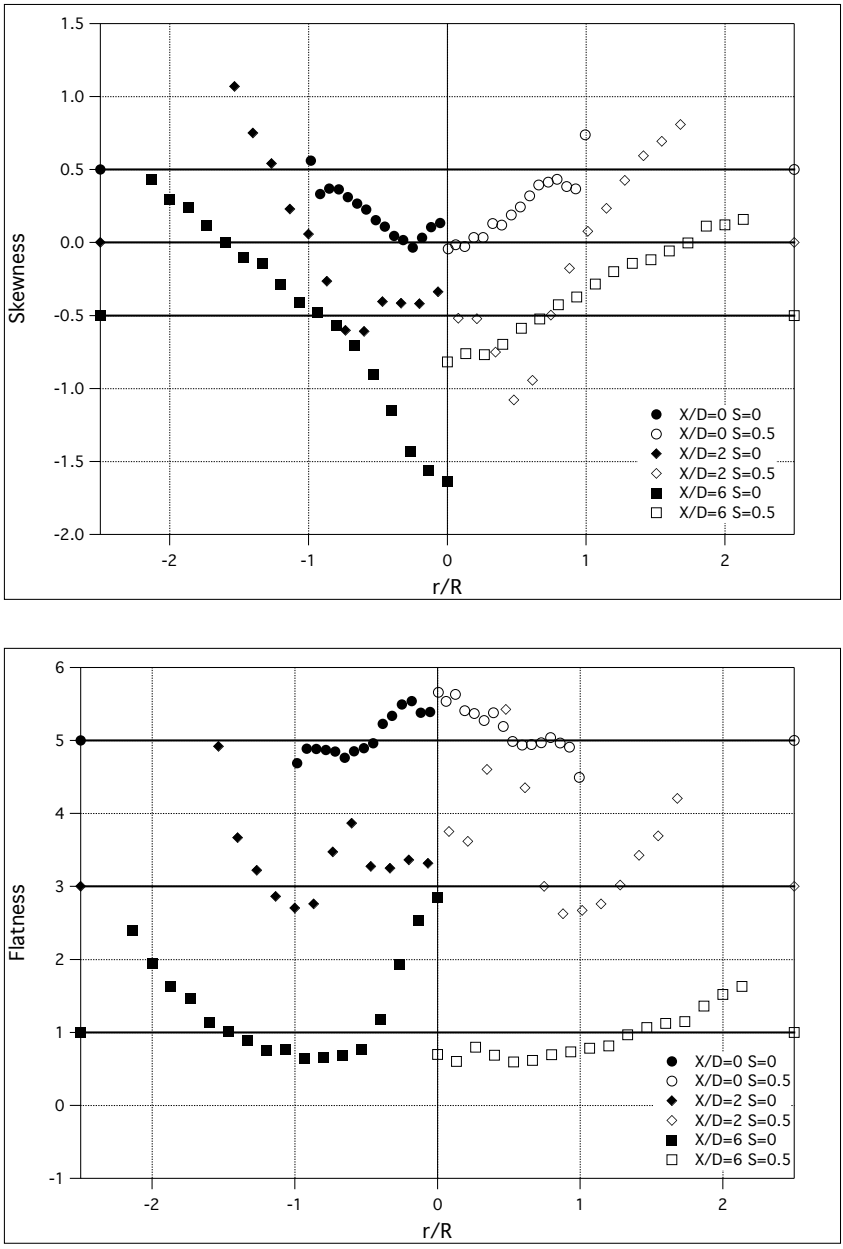

FIGURE 6.8. Skewness (a) and flatness (b) of the axial velocity at Re=24000 for three different x–positions and with S=0 and 0.5. Note that the profiles have been shifted in the vertical direction. The thick horizontal lines show the where the skewness and flatness are 0 and 3, respectively.

6.2.2. *Azimuthal and radial velocity fluctuations*

The development of turbulence level of the azimuthal and radial velocity components for Re=24000 and S=0.5 are shown in figures 6.9 and 6.10. In fact both distributions are similar to the distributions for u_{rms} (see figure 6.7) although the level of the fluctuations are lower.

The skewness and flatness reveal some more details of the jet structure (see figures 6.11 and 6.12). For both components the skewness is antisymmetric around the centre which is what one would expect for an axisymmetric flow. At x/D=2 the skewness for v shows a local maximum (minimum) at $|r/R| \approx$ 0.8. This is most probably an effect of the instability affecting the potential core. It is interesting to note that this position does not correspond to the maximum in the rms, in fact the maximum in rms is approximately where the skewness is zero. Similar local extreme values is observed also for the radial component at x/D=2. However at x/D=6 the distribution of the skewness for the two components are quite different. The azimuthal component show an almost constant level of zero except at the outermost points. This seems to indicate an almost Gaussian distribution of the fluctuations which is also substantiated by the flatness which is close to 3. However the skewness for the radial component increases (decreases) almost linearly with r indicating regions of large fluctutations directed towards the centre. A similar effect is seen in the flatness with fairly large values in the outer part of the jet.

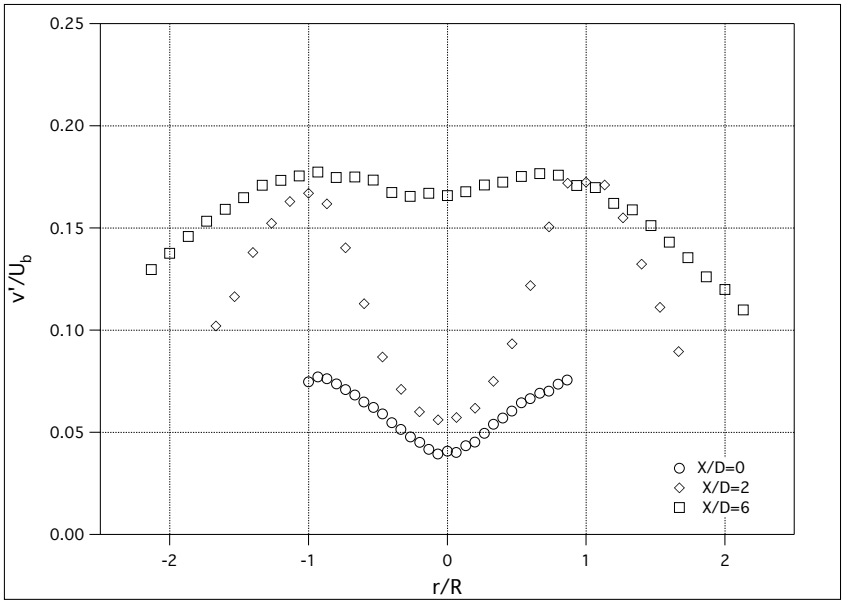

FIGURE 6.9. Azimuthal turbulence intensity at Re=24000, S=0.5, see fig 6.1 for symbols.

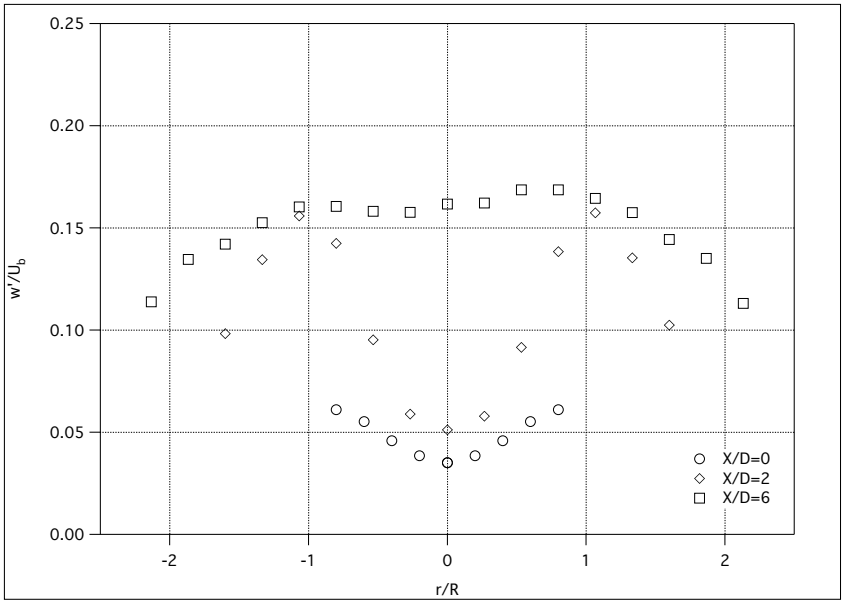

FIGURE 6.10. Radial turbulence intensity at Re=24000, S=0.5.

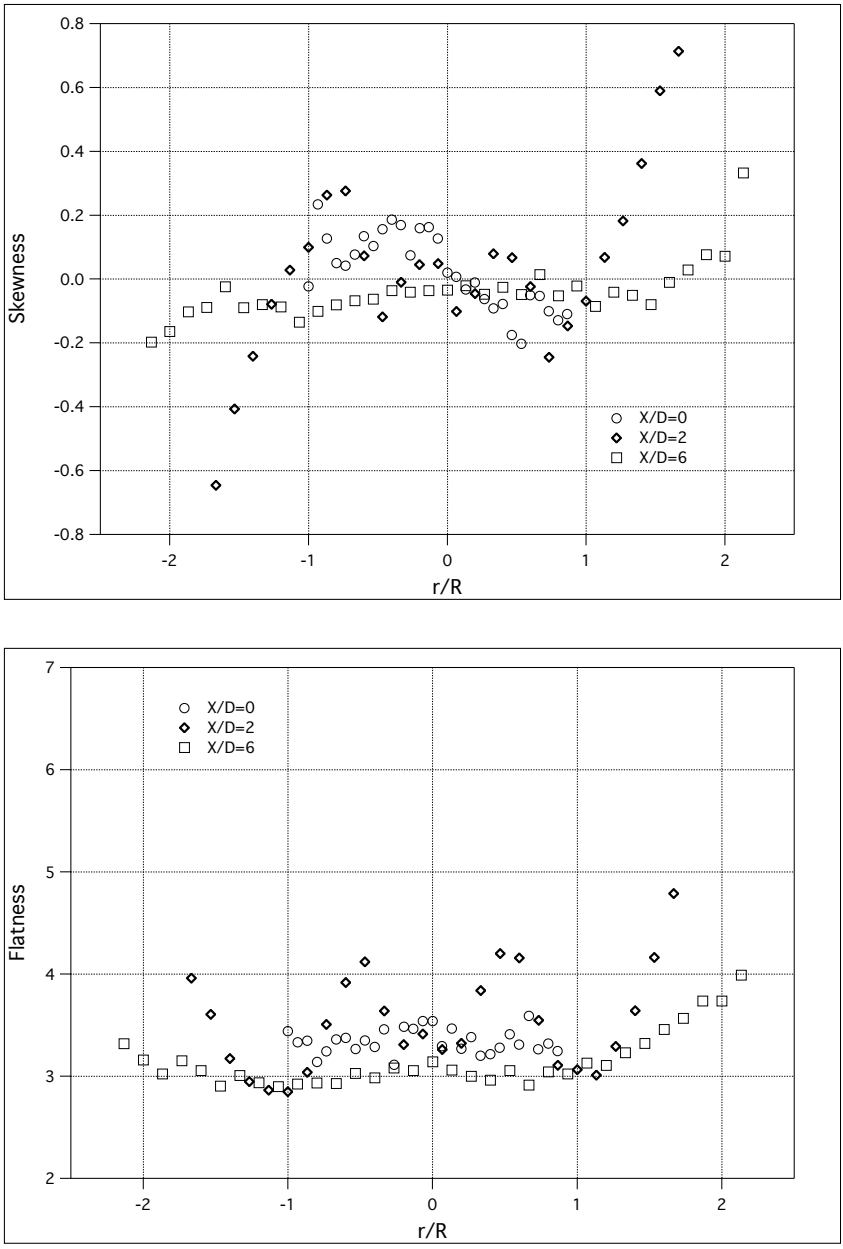

FIGURE 6.11. Skewness (a) and flatness (b) of azimuthal velocity at Re=24000, S=0.5.

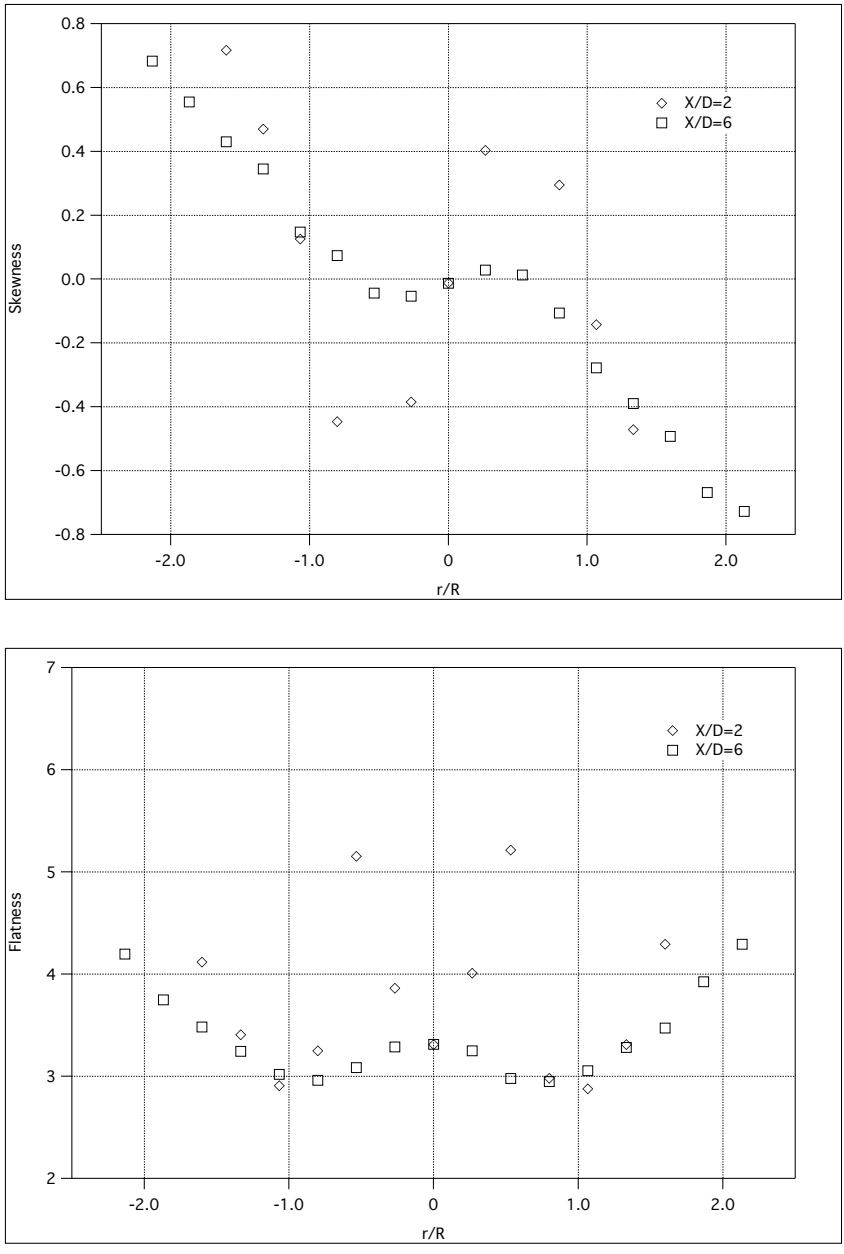

FIGURE 6.12. Skewness (a) and flatness (b) of radial velocity at Re=24000, S=0.5.

6.2.3. *Axial development of turbulence*

The variation of the turbulence level on the centreline as function of the downstream distance is shown in figures 6.13 and 6.14. Data were obtained for the three Reynolds numbers (12000, 24000 and 33500) and three values of the swirl number (0, 0.2 and 0.5). The data presented in the two figures were obtained with LDV and hot-wire anemometry, respectively. There are of course also data for the streamwise fluctuations available from the hot-wire measurements and they are in good agreement with the LDV-data (at worst a 10% difference). We therefore restrict ourselves to present only the LDV-data in figure 6.13.

The variation of the turbulence level of the axial component (u'/U_b) along the x-axis, is shown in figure 6.13a–c. The turbulence level close to the outlet is only weakly affected by Reynolds number and swirl rate. There is also an initial region where there is only a weak increase in the turbulence level (up to x/D=2–3). We have earlier denoted this the "potential" core region. Downstream this region the turbulence level increases significantly, reaches a maximum around x/D=6 and then decreases. The curves seem to cross around $x/D = 10$. It is clearly seen that the onset of the increase in turbulence level moves upstream as the swirl is increased due to the enhanced mixing (with the associated decrease in core length) and that the maximum of the turbulence moves likewise. However the axial position of the peak is almost constant for each swirl rate irrespectively of the Reynolds number. All in all one may say that for the present Reynolds number range there is a very small variation in the beaviour of the turbulence at the centreline. Finally we have included data from Rose (1962) in figure 6.13a. For the non-rotating case these data overlap with the present data, for the rotating case the data of Rose (1962) show an even larger effect of the rotation than in our case. To some extent this may be due to the fact that their swirl number was 0.6 as compared to the highest in the present study which was 0.5.

In figure 6.14 the axial development at the centreline of the turbulence level for the orthogonal component v'/U_b.[1] These data show a similar picture as for the u_{rms}-data, there is only a small influence of the Reynolds number, but a significant influence of the swirl. It can also be noted that the initial increase of v_{rms} seem to start somewhat closer to the exit than for the streamwise fluctautions. This may be due to the fact that even in the potential core large scale structures in the outer region may give a "buffeting" to the core which give rise to fluctuations in a plane normal to the streamwise direction.

[1]We chose to call this component "orthogonal" at the centreline since the azimuthal component is not well defined there.

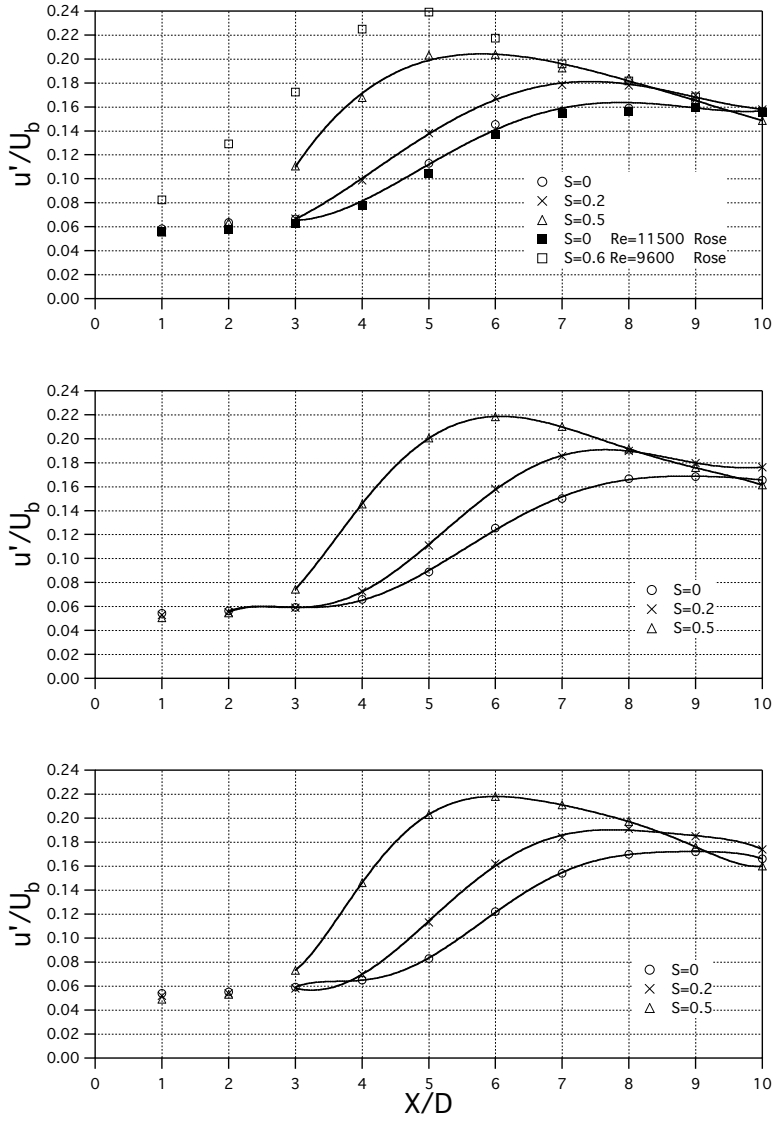

FIGURE 6.13. Turbulence intensity of the streamwise velocity component at the centreline, a) Re=12000, also includes data from Rose (1962), b) Re=24000, c) Re=33500. Full lines are for visual aid only.

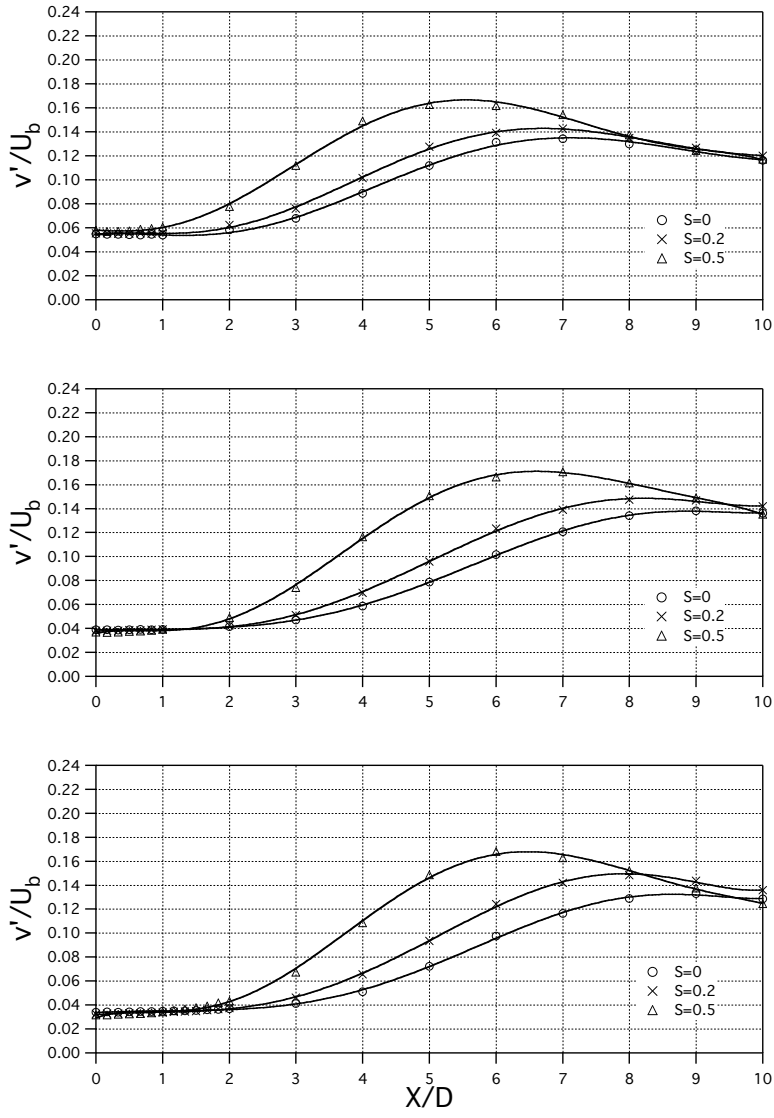

FIGURE 6.14. Turbulence intensity of the orthogonal velocity component at the centreline, a) Re=12000, b) Re=24000, c) Re=33500. Full lines are for visual aid only.

6.2.4. *Spectral information*

The flow field in the near-exit region of the jet is quite complex and in order to understand the development of the flow structures time resolved measurements as well as two-point measurements are needed to get the temporal and spatial evolution of the flow field. This is beyond the scope of the present work but in order to give some information concerning the vortical structures we will present a few results obtained from spectral analysis. For this analysis we use hot-wire anemometry data which was collected by an X-probe. The data were taken at the centreline at x/D=2 and 6 and for a Re=33500 and both the streamwise (u) and the orthognal (v) components were analysed. The spectra are shown in figures 6.15 and 6.16.

Figure 6.15a shows that at x/D=2 a distinct peak in the u-components is detected for all three swirl numbers. If the frequency is normalised by the bulk velocity and pipe diameter, a Strouhal number of about 0.5 is obtained, which remains constant for all swirl numbers studied here. This peak is also present at the other Reynolds number studied. The St-value of 0.5 is within the range of values reported in previous studies (see section 3.1.1). It is interesting to compare with the spectra measured at the pipe outlet which show no evidence of a similar peak (see figure 5.7).

Since the spectra here are plotted in such a way that the area under the spectra is directly proportional to the energy content of the signal it is clear that the rms for the three signals are fairly similar although the S=0 case is the one with the largest rms (cf. figure 6.13c). However in figure 6.15b we see a dramatic change in the spectra. First of all there is now large differences in energy content between the three different swirl numbers, and in contrast to the situation at x/D=2 the S=0.5 case shows the largest energy. The distinct peak that previously was easily seen has also disappeared and the spectra now has a broad band character. The maximum varies between St=0.35 for S=0.5 to St=0.55 for S=0. The broadening of the spectra is due to the interaction and breakdown of the structures and the spectra obtain a shape which is typical for turbulent jets.

Also the spectra (figure 6.16) of the orthogonal component show a similar behaviour, however at x/D=2 the largest peak is seen for S=0.5. In this case the Strouhal number of the peak seem to change somewhat with S. At x/D=6 the spectra broadens much in the same way as was observed for the spectra for the streamwise component.

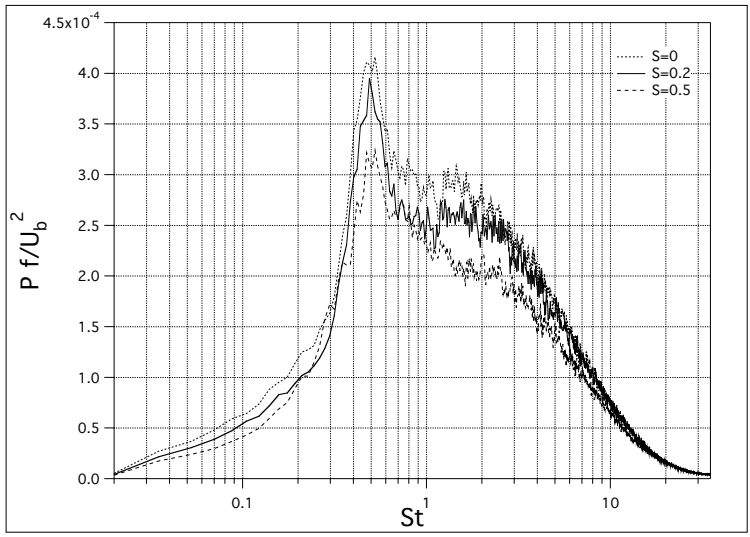

a)

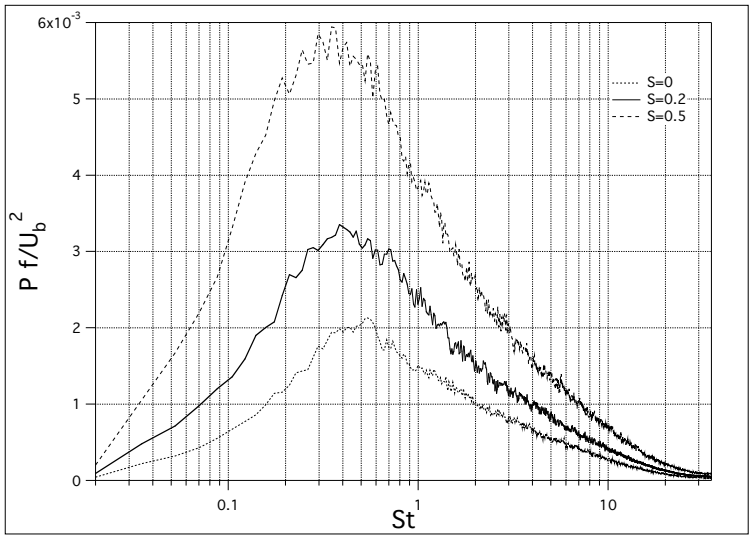

b)

FIGURE 6.15. Spectra of u-component at centreline for Re=33500. a) x/D=2, b) x/D=6.

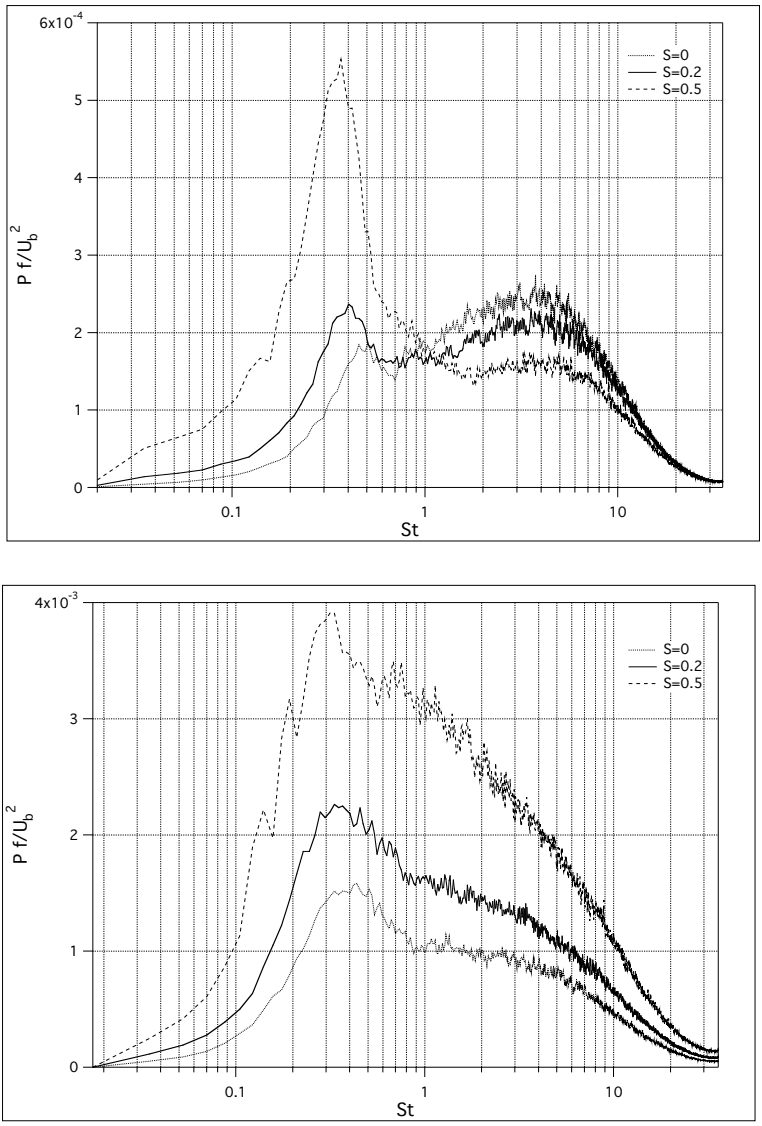

FIGURE 6.16. Spectra of v-component at centreline for Re=33500. a) x/D=2, b) x/D=6.

6.3. Instantaneous flow angle measurements

Free shear flows may show large instantaneous flow angles and in some cases even back flow. This is the case in for instance the outer region of jet flows. In the following we present some results to illustrate this and also give a comparison between the LDV and hot-wire techniques used in the present study.

An illustration of the behaviour of the flow angle is to plot the instantaneous measured points directly on the calibration region (see figure 6.17). As can be seen the calibration curve is limited to $\pm 40°$. The data in the figure are taken at r/R=0.335 for two swirl numbers (S=0 and 0.5) and it is possible to follow the evolution of the cloud of points for different downstream positions (x/D=0, 2, 6). In all the figures the same amount (1600 measured points) of experimental data is plotted. For x/D=0 and x/D=2, the swirl shifts the points towards a higher axial velocity and at the same time the azimuthal component gives a shift of the cloud from the zero-angle line. At x/D=6 an opposite effect on the axial component is observed, i.e. the axial velocity has decreased. Clearly, moving downstream, the cloud spreads and its covered area in the calibration curve is enlarged. With swirl the growth of this area becomes larger. In the case of x/D=6 it is possible to register some data points which lie outside the region limited by the calibration.

Figures 6.18 and 6.19 show the mean angle at the pipe outlet (x/D=0) measured with the X-probe and the LDV, respectively. The data are all for S=0.5, but for the three different Reynolds numbers. As can be seen there is only a small difference between the different Re as was expected. It should be noted that the hot-wire measurements were corrected according to the procedure described in section 4.2.2.

In figure 6.20 the data from the two different techniques at Re=24000 are directly compared and it is seen that the agreement is nearly perfect. In this figure we also plotted the uncorrected hot-wire data. As expected the largest corrections occur in the outer part of the jet, however they are still fiarly small.

Figure 6.21 plot the mean and 99% interval of the instantaneous angle measured with the hot-wire. In the figures three groups of lines, marking different downstream positions, are plotted. The central curve of each group corresponds to the mean value of the flow angle as already shown in figures 6.18 and 6.19. The upper and lower curves display the region for which 99% of the data are located (i.e. at each side of these lines 0.5% of the data are found).

When moving downstream, the mean flow angle between the axial and azimuthal velocity components decreases. At the same time the angle interval is amplified especially in the outer radial positions. Moreover, from the figure itself it is possible to note that the probability density function is skewed since the upper and the lower curves are not equally distanced from the mean curve. Even if the mean values are relatively small, the lines of 99% interval can exceed the range of the calibration curve ($\pm 40°$) due to the large fluctuations present in the flow.

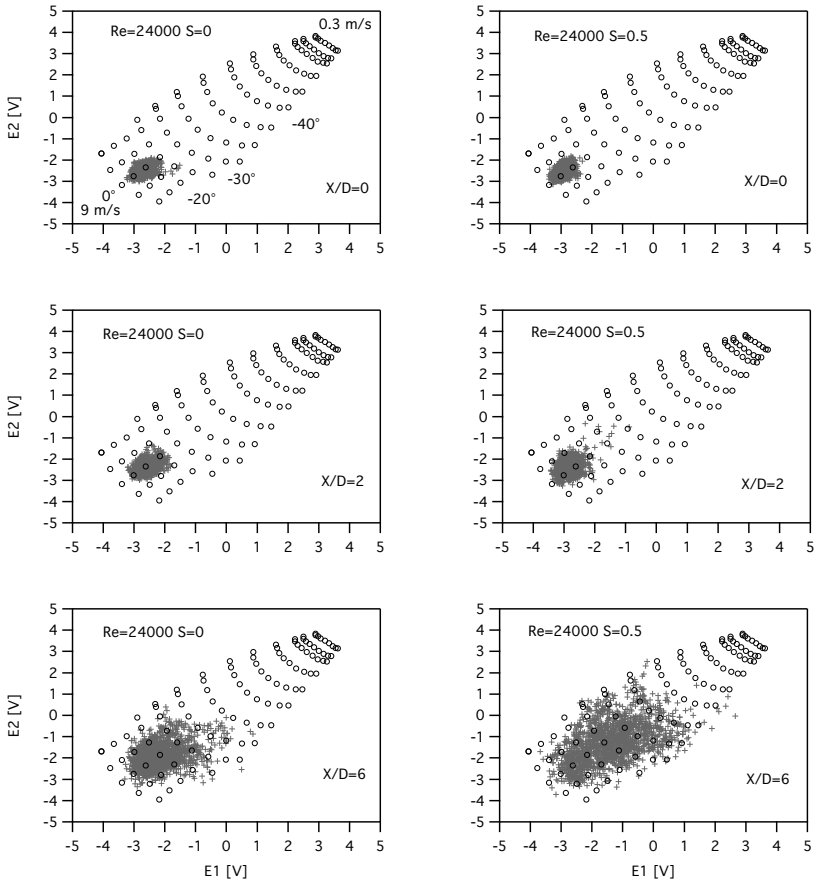

FIGURE 6.17. Hot-wire calibration region with instantaneous measurement data.

Finally it can be noted that at x/D=6 it seems that the mean flow angle in the central region changes sign. This corresponds to what was observed in figure 6.2 which was measured with LDV. If this is a physical behaviour or a measurement problem is not clear and should be further investigated.

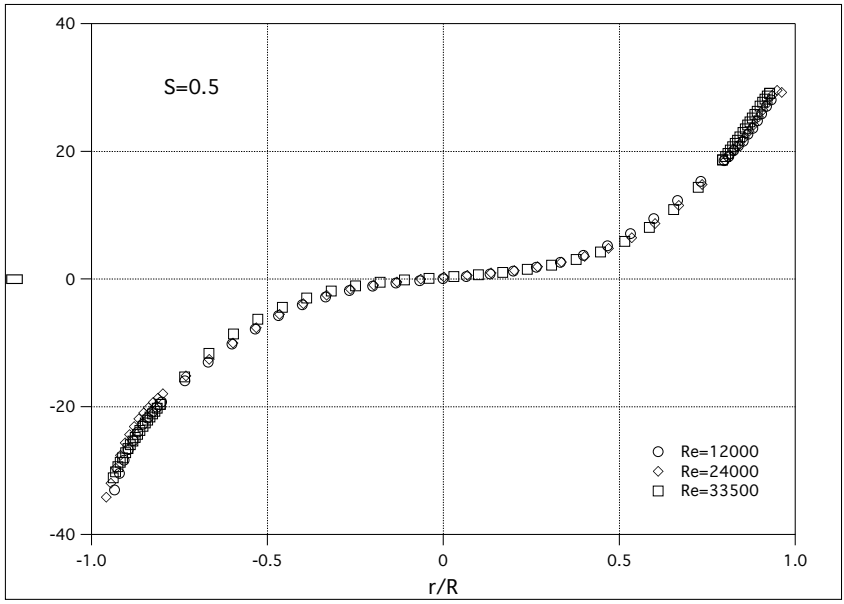

FIGURE 6.18. Flow angle between axial and azimuthal mean velocity components at the pipe exit measured with X-probe.

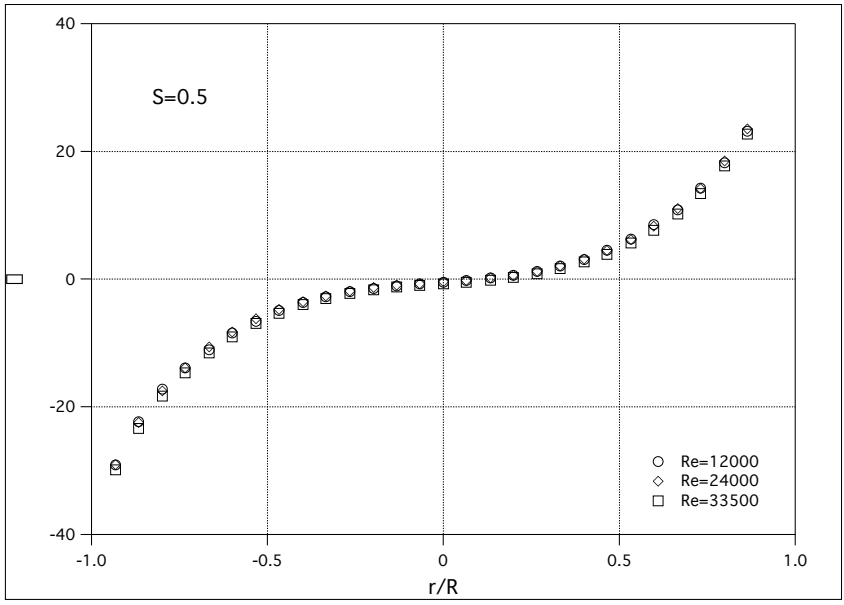

FIGURE 6.19. Flow angle between axial and azimuthal mean velocity components at the pipe exit measured with LDV.

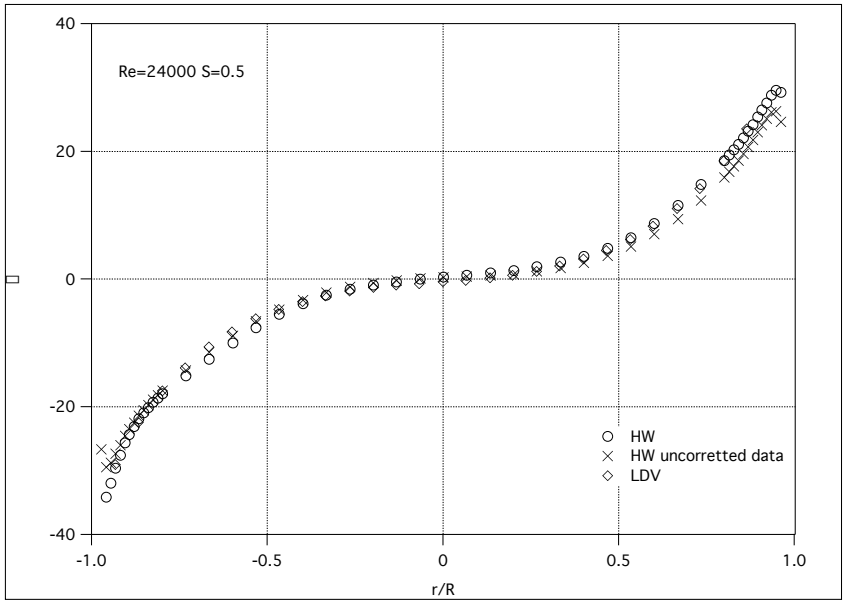

FIGURE 6.20. Comparison between the flow angles in figures 6.18 and 6.19 for Re=24000.

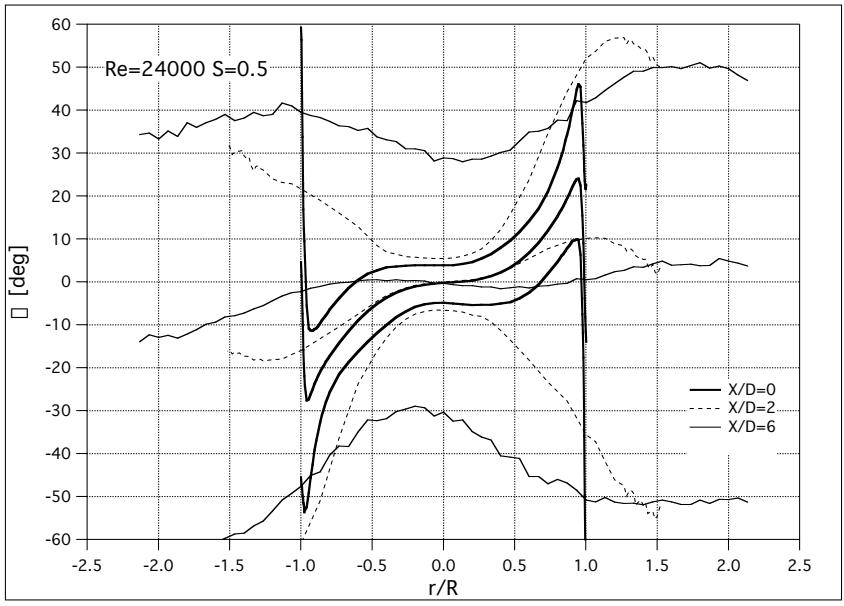

FIGURE 6.21. Mean and 99% interval for the angle between axial and azimuthal instantaneous velocity at Re=24000 S=0.5 measured with hot-wire anemometry for x/D=0, 2 and 6.

CHAPTER 7

Summary and conclusions

The experimental work has been aimed towards the investigation of rotating flows, both a turbulent rotating pipe flow as well as swirling jet flow. An experimental set-up has been designed which has been shown to give a fully developed turbulent pipe flow. Particular attention has been paid during the design and the construction of the set-up in order to have a high quality flow with a low level of disturbances coming from the upstream conditions or vibrations of the pipe. For the jet experiments this is highly valuable since the exit conditions can be viewed as independent of the geometry which would not be the case using swirl generators or adding secondary injection flows.

The flow field has been investigated using both hot-wire anemometry and LDV. In cases where comparisons have been possible there is a good correspondence between the two methods.

The parameter space for the experiments is defined by the Reynolds number and the swirl number. For swirl numbers up to 0.5, the Reyolds number has been varied between 12000 and 33500, whereas the pipe flow has been studied for swirl numbers up to 1.5 at a Re=12000.

The jet was studied in the near exit region, up to 10 diameters from the exit plane. Both the mean flow and the fluctuating velocity components were measured.

The following points highlights the findings of the present work:

Turbulent pipe flow

• The change of the axial profile towards a parabolic shape was verified when rotation is applied.

• Accurate measurements of the azimuthal profile shows a parabolic shape independent of Re for $S > 0$.

• An expression for the $\overline{vw}$ Reynolds stress term has been derived under the assumption that the azimuthal velocity is parabolic. It is shown to vary linearly with r.

• The mean flow data were compared with recent theoretical scaling results of Oberlack (1999). The experimental results seem to follow the theoretical results closely, although more work is needed to fully verify all parts of the theory.

Swirling jet flow

• All three velocity components were measured in the near field of a swirling jet.

• Flow entrainment measurements show that the entrainment decreases with rotation as compared with the non-rotation case, despite the fact that rotation makes the potential core break down faster.

• An interesting, so far unexplained, result is that the azimuthal velocity seems to have changed sign in the core of the jet at x/D=6. This is observed both in hot-wire and LDV measurements.

• The measurements of the radial velocity component seem to indicate fairly high negative velocities towards the jet centreline, although the mean flow is directed outwards.

Acknowledgements

This research has been sponsored by the Swedish Energy Agency (STEM). The support is greatefully acknowledged.

First of all I would like to thank my supervisor Prof. Henrik Alfredsson who always supported me and "trusted" my ideas helping me with fruitful discussions and suggestions.
I want to acknowledge Nils Tillmark for his great availability and help in solving everyday problems and Alessandro Talamelli for his fundamental contribution to the work.
I also want to thank Prof. Bengt Sundén and the groups working at Lund Institute of Technology for their collaboration.

A special thank to Marcus Gällstedt and Ulf Landén for their many high quality works in the workshop.
I want to name Gunnar Wingstedt who helpfully gave us the framework for the experimental setup.

I am very thankful towards my friends and office-mates Davide Medici and Junichiro Shiomi who have been and are always ready to share the bad and the good time with me.
I would like to thank my professors and colleagues at KTH Mekanik who create a pleasant and friendly environment. Special thanks to Dr. Fredrik Lundell for all his advises and helpfully suggestions.

Of course I can not forget all the friends that supported me during all this time in Sweden. I am specially grateful to all the members of Cmis.

To the Isacson family which adopted me like a son, I thank you from the bottom of my heart.

Un grazie alla mia famiglia che mi é sempre stata vicina e si è sempre tenuta informata sul "sarchia".
Grazie a chi é riuscita a riempire di sé tutti i miei pensieri.

Bibliography

Abramovich, G. N. 1963 *The theory of turbulent jets*. MIT Press.

Alfredsson, P. H. & Johansson, A. V. 1982 Experimental studies of turbulent channel flow. Technical Report, Dept. Mechanics, KTH, Stockholm, Sweden.

Barnes, D. & Kerswell, R. 2000 New results in rotating Hagen-Poiseuille flow. *J. Fluid Mech.* **417**, 103–126.

Beér, J. M. & Chigier, N. A. 1972 *Combustion aerodynamics*. Applied Science Publishers LTD, London.

Billant, P., Chomaz, J.-M. & Huerre, P. 1998 Experimental study of vortex breakdown in swirling jets. *J. Fluid Mech.* **376**, 183–219.

Bradshaw, P. 1969 The analogy between streamline curvature and buoyancy in turbulent shear flow. *J. Fluid Mech.* **36**, 177–191.

Chigier, N. A. & Chervinsky, A. 1967 Experimental investigation of swirling vortex motion in jets. *J. Appl. Mech.* **34**, 443–451.

Eggels, J. 1994 Direct and large eddy simulation of turbulent flow in a cylindrical pipe geometry. PhD thesis, Delft University of Technology, The Netherlands.

Eggels, J. G. M., Unger, F., Weiss, M. H., Westerweel, J., Adrian, R. J., Friedrich, R. & Nieuwstadt, F. T. M. 1994 Fully developed turbulent pipe flow: a comparison between direct numerical simulation and experiment. *J. Fluid Mech.* **268**, 175–209.

Facciolo, L., Tillmark, N. & Talamelli, A. 2003 Experimental investigation of jets produced by rotating fully developed pipe flow. In *Proc. Third Int. Symp. Turbulence and Shear Flow Phenomena, Sendai*, pp. 1217–1222.

Farokhi, S., Taghavi, R. & Rice, E. J. 1988 Effect of initial swirl distribution on the evolution of a turbulent jet. *AIAA J.* **27**, 700–706.

Farokhi, S., Taghavi, R. & Rice, E. J. 1992 Modern development in shear flow control with swirl. *AIAA J.* **30**, 1482–706.

Feiz, A., Ould-Rouis, M. & Lauriat, G. 2003 Large eddy simulation of turbulent flow in a rotating pipe. *Int. J. Heat Fluid Flow* **24**, 412–420.

Hirai, S., Takagi, T. & Matsumoto, M. 1988 Predictions of the laminarization phenomena in an axially rotating pipe flow. *J. Fluids Engng.* **110**, 424–430.

Howard, L. & Gupta, A. 1962 On the hydrodynamic and hydromagnetic stability of swirling flows. *J. Fluid Mech.* **14**, 463–476.

Hu, G.-H., Sun, D.-J. & Yin, X.-Y. 2001 A numerical study of dynamics of a temporally evolving swirling jet. *Phys. Fluids* **13**, 951–965.

Hussain, A. K. M. F. 1986 Coherent structures and turbulence. *J. Fluid Mech.* **173**, 303–356.

Imao, S., Itoh, M. & Harada, T. 1996 Turbulent characteristics of the flow in an axially rotating pipe. *Int. J. Heat Fluid Flow* **17**, 444–451.

Imao, S., Itoh, M., Yamada, Y. & Zhang, Q. 1992 The characteristics of spiral waves in an axially rotating pipe. *Exp. Fluids* **12**, 277–285.

Khorrami, M. R. 1995 Stability of a compressible axisymmetric swirling jet. *AIAA J.* **4**, 650–658.

Kikuyama, K., Murakami, M., Nishibori, K. & Maeda, K. 1983 Flow in an axially rotating pipe. *Bull. JSME* **26**, 506–513.

Komori, S. & Ueda, H. 1985 Turbulent flow structure in the near field of a swirling round free jet. *Phys. Fluids* **28**, 2075–2082.

Kurbatskii, A. & Poroseva, S. 1999 Modeling turbulent diffusion in a rotating cylindrical pipe flow. *Int. J. Heat and Fluid Flow* **20**, 341–348.

Leibovich, S. & Stewartson, K. 1983 A sufficient condition for the instability of columnar vortices. *J. Fluid Mech.* **126**, 335–356.

Lessen, M. & Paillet, F. 1974 The stability of a trailing line vortex. Part 2. Viscous theory. *J. Fluid Mech.* **65**, 769–779.

Lessen, M., Singh, P. J. & Paillet, F. 1974 The stability of a trailing line vortex. Part 1. Inviscid theory. *J. Fluid Mech.* **63**, 753–763.

Liepmann, D. & Gharib, M. 1992 The role of streamwise vorticity in the near-field entrainment of round jets. *J. Fluid Mech.* **245**, 643–668.

Lilley, D. G. 1999 Annular vane swirler performance. *J. Propul. Power* **15**, 248–252.

Lim, D. W. & Redekopp, L. G. 1998 Absolute instability conditions for variable density, swirling jet flows. *Eur. J. Mech. B/Fluids* **17**, 165–185.

Loiseleux, T. & Chomaz, J. M. 2003 Breaking of rotational symmetry in a swirling jet experiment. *Phys. Fluids* **15**, 511–523.

Loiseleux, T., Chomaz, J. M. & Huerre, P. 1998 The effect of swirl on jets wakes: Linear instability of the rankine vortex with axial flow. *Phys. Fluids* **10**, 1120–1134.

Malin, M. & Younis, B. 1997 Prediction of turbulent transport in an axially rotating pipe. *Int. Comm. Heat Mass Transfer* **24**, 89–98.

Martin, J. E. & Meiburg, E. 1994 On the stability of the swirling jet shear layer. *Phys. Fluids* **6**, 424–426.

Martin, J. E. & Meiburg, E. 1998 The growth and nonlinear evolution of helical perturbations in a swirling jet model. *Eur. J. Mech. B/Fluids* **17**, 639–651.

Maslowe, S. 1974 Instability of rigidly rotating flows to non-axisymmetric disturbances. *J. Fluid Mech.* **64**, 307–317.

Mayer, E. W. & Powell, K. G. 1992 Similarity solutions for viscous vortex cores. *J. Fluid Mech.* **238**, 487–507.

McIlwain, S. & Pollard, A. 2002 Large eddy simulation of the effects of mild swirl on the near field of a round free jet. *Phys. Fluids* **14**, 653–661.

Metha, R. D., Wood, D. H. & Clausen, P. D. 1991 Some effects of swirl on turbulent mixing layer development. *Phys. Fluids A* **3**, 2716–2724.

Michalke, A. 1984 Survey on jet instability theory. *Prog. Aerospace Sci.* **21**, 159–199.

Michalke, A. 1999 Absolute inviscid instability of a ring jet with back-flow and swirl. *Eur. J. Mech. B/Fluids* **18**, 3–12.

Murakami, M. & Kikuyama, K. 1980 Turbulent flow in axially rotating pipes. *J. Fluids Eng.* **102**, 97–103.

Nagib, H., Lavan, Z. & Fejer, A. 1971 Stability of pipe flow with superposed solid body rotation. *Phys. Fluids* **14**, 766–768.

Oberlack, M. 1999 Similarity in non-rotating and rotating turbulent pipe flows. *J. Fluid Mech.* **379**, 1–22.

Oberlack, M. 2001 A unified approach for symmetries in plane parallel turbulent shear flows. *J. Fluid Mech.* **427**, 299–328.

Orlandi, P. 1997 Helicity fluctuations and turbulent energy production in rotating and non-rotating pipes. *Phys. Fluids* **9**, 2045–2056.

Orlandi, P. & Ebstein, D. 2000 Turbulent budgets in rotating pipes by DNS. *Int. J. Heat Fluid Flow* **21**, 499–505.

Orlandi, P. & Fatica, M. 1997 Direct simulations of turbulent flow in a pipe rotating about its axis. *J. Fluid Mech.* **343**, 43–72.

Österlund, J. M. 1999 Experimental studies of zero pressure-gradient turbulent boundary layer flow. PhD thesis, TRITA-MEK Tech. Rep. 1999:16, Dept. Mech., KTH, Stockholm, Sweden.

Panda, J. & McLaughlin, D. K. 1994 Experiments on the instabilities of a swirling jet. *Phys Fluids* **6**, 263–276.

Park, S. H. & Shin, H. D. 1993 Measurement of entrainment characteristics of swirling jets. *Int. J. Heat Mass Tran* **136**, 4009–4018.

Pedley, T. 1968 On the instability of rapidly rotating shear flows to non-axisymmetric disturbances. *J. Fluid Mech.* **31**, 603–607.

Pedley, T. 1969 On the instability of viscous flow in a rapidly rotating pipe. *J. Fluid Mech.* **35**, 97–115.

Pratte, B. D. & Keffer, J. F. 1972 The swirling turbulent jet. *J. Basic Eng., Trans. ASME* **93**, 739–748.

Rahai, H. R. & Wong, T. W. 2001 Velocity field characteristics of turbulent jets from round tubes with coil inserts. *Appl. Thermal Eng.* **22**, 1037–1045.

Reich, G. & Beer, H. 1989 Fluid flow and heat transfer in an axially rotating pipe –I. Effect of rotation on turbulent pipe flow. *Int. J. Heat Mass Transfer* **32**, 551–562.

Rinck, K.-J. & Beer, H. 1998 Numerical calculation of the fully developed turbulent flow in an axially rotating pipe with a second-moment closure. *J. Fluids Engng.* **120**, 274–279.

Rose, W. G. 1962 A swirling round turbulent jet. *J. Appl. Mech.* **29**, 615–625.

Satake, S. & Kunugi, T. 2002 Direct numerical simulation of turbulent heat transfer in an axially rotating pipe flow. Reynolds shear stress and scalar flux budgets. *Int. J. Num. Methods Heat Fluid Flow* **12**, 958–1008.

Sislian, J. P. & Cusworth, R. A. 1986 Measurements of mean velocity and turbulent intensities in a free isothermal swirling jet. *AIAA J.* **24**, 303–309.

Speziale, C., Younis, B. & Berger, S. 2000 Analysis and modelling of turbulent flow in an axially rotating pipe. *J. Fluid Mech.* **407**, 1–26.

Talamelli, A., Westin, K. J. A. & Alfredsson, P. A. 2000 An experimental

investigation of the response of hot wire X-probes in shear flows. *Exp. Fluids* **23**, 425–435.

Thomas, F. O. 1991 structure of mixing layers and jets. *Appl. Mech. Rev.* **44**, 119–153.

Toplosky, N. & Akylas, T. 1988 Nonlinear spiral waves in rotating pipe flow. *J. Fluid Mech.* **190**, 39–54.

Wallin, S. & Johansson, A. 2000 An explicit algebraic Reynolds stress model for incompressible and compressible turbulent flow. *J. Fluid Mech.* **403**, 89–132.

Weigand, B. & Beer, H. 1994 On the universality of the velocity profiles of a turbulent flow in an axially rotating pipe. *Appl. Sci. Res.* **52**, 115–132.

White, A. 1964 Flow of a fluid in an axially rotating pipe. *J. Mech. Engng. Sci.* **6**, 47–52.

Yang, Z. 2000 Large eddy simulation of fully developed turbulent flow in a rotating pipe. *Int. J. Numer. Meth. Fluids* **33**, 681–694.